

BRNO UNIVERSITY OF TECHNOLOGY

Faculty of Electrical Engineering  
and Communication

MASTER'S THESIS

Brno, 2024

Bc. David Sedláček



# BRNO UNIVERSITY OF TECHNOLOGY

VYSOKÉ UČENÍ TECHNICKÉ V BRNĚ

## FACULTY OF ELECTRICAL ENGINEERING AND COMMUNICATION

FAKULTA ELEKTROTECHNIKY  
A KOMUNIKAČNÍCH TECHNOLOGIÍ

## DEPARTMENT OF RADIO ELECTRONICS

ÚSTAV RADIOELEKTRONIKY

## SOFTWARE-DEFINED ANTENNA ARRAY

SOFTWAREVĚ DEFINOVANÁ ANTÉNNÍ ŘADA

### MASTER'S THESIS

DIPLOMOVÁ PRÁCE

### AUTHOR

AUTOR PRÁCE

**Bc. David Sedláček**

### SUPERVISOR

VEDOUCÍ PRÁCE

**prof. Ing. Roman Maršálek, Ph.D.**

**BRNO 2024**

# Master's Thesis

Master's study program **Space Applications**

Department of Radio Electronics

**Student:** Bc. David Sedláček

**ID:** 221347

**Year of  
study:** 2

**Academic year:** 2023/24

**TITLE OF THESIS:**

## Software-defined antenna array

### INSTRUCTION:

The goal of the thesis is to build a demonstrator of a coherent multi-channel radio, including implementation of signal processing algorithms related to digital beamforming in antenna arrays such as direction of arrival (DoA) estimation and electronic beam steering. The work is motivated by R&D activities in company Groundcom.space related to modern antennas for satellite communications.

Review the available solutions for multichannel software defined radio (SDR) modules and analyze the trade-offs of the different approaches – full off-the-shelf solutions vs. external phase synchronization. Select the most suitable platform. Implement and validate the DoA and beam-forming algorithms (such as MUSIC, MVDR), first in SW and then on the selected SDR platform. Evaluate the computational resources needed and discuss possible real-time operation. Define the testing scenarios for laboratory testing and metrics that will define successful commissioning of the device. Build and calibrate a testbed that will allow to test the accuracy for multiple directions of arrival. Conduct the testing campaign and critically evaluate the results.

### RECOMMENDED LITERATURE:

- [1] Travis Collins; Robin Getz; Alexander Wyglinski; Di Pu, Software-Defined Radio for Engineers , Artech, 2018.
- [2] M. Laakso, R. Rajamäki, R. Wichman and V. Koivunen, "Phase-coherent multichannel SDR - Sparse array beamforming," 2020 28th European Signal Processing Conference (EUSIPCO), Amsterdam, Netherlands, 2021, pp. 1856-1860, doi: 10.23919/Eusipco47968.2020.9287664.

**Date of project  
specification:** 16.2.2024

**Deadline for  
submission:** 20.5.2024

**Supervisor:** prof. Ing. Roman Maršálek, Ph.D.

**Consultant:** Ing. Jan Vélím

**doc. Ing. Tomáš Götthans, Ph.D.**  
Chair of study program board

### WARNING:

The author of the Master's Thesis claims that by creating this thesis he/she did not infringe the rights of third persons and the personal and/or property rights of third persons were not subjected to derogatory treatment. The author is fully aware of the legal consequences of an infringement of provisions as per Section 11 and following of Act No 121/2000 Coll. on copyright and rights related to copyright and on amendments to some other laws (the Copyright Act) in the wording of subsequent directives including the possible criminal consequences as resulting from provisions of Part 2, Chapter VI, Article 4 of Criminal Code 40/2009 Coll.

## **ABSTRACT**

The main objective of this thesis was to develop a demonstrator platform implementing signal processing algorithms for signal direction of arrival estimation. In total, six estimation techniques were described, and simulations of discussed beamforming and subspace-based methods were implemented in Python. A study was conducted on available hardware, comparing trade-offs between customised and off-the-shelf solutions. Specific hardware and software configurations were proposed for practical implementation of the estimation methods. Finally, a testbed was constructed to verify the performance of the implemented estimation methods. Tests were performed, and the results were critically evaluated.

## **KEYWORDS**

Antenna array, digital signal processing, direction-of-arrival estimation, MUSIC, software-defined radio, KrakenSDR, Python

## **ABSTRAKT**

Hlavným cieľom tejto práce bolo vyvinúť demonštračnú platformu pre implementáciu algoritmov na odhad smeru príchodu signálu. Celkovo bolo opísaných šesť techník, ktoré boli následne implementované v Pythone spolu so simuláciami príchodu signálov. Bola vykonaná štúdia dostupného hardvéru, v ktorej boli porovnané rozdiely medzi na mieru prispôbenými a voľne dostupnými riešeniami. Navrhli sa konkrétne hardvérové a softvérové konfigurácie pre praktickú implementáciu metód odhadu príchodu signálu. Na záver boli navrhnuté experimentálne merania na overenie účinnosti implementovaných metód. Vykonali sa testovacie merania a ich výsledky boli kriticky zhodnotené.

## **KLÍČOVÁ SLOVA**

Anténne pole, digitálne spracovanie signálov, odhad smeru príchodu, MUSIC, softvérovo definované rádio, KrakenSDR, Python

SEDLÁČEK, David. *Software-defined antenna array*. Master's Thesis. Brno: Brno University of Technology, Faculty of Electrical Engineering and Communication, Department of Radio Electronics, 2034. Advised by prof. Ing. Roman Maršálek, Ph.D.

# Rozšírený abstrakt

Počiatky odhadu smeru príchodov signálov sa dajú datovať až ku raným experimentom zameraným na zameriavanie polohy mobilných zariadení počas tiesňových volaní. Od týchto prvotných pokusov našli techniky pre odhad príchodu rádiových signálov (ďalej len “odhad DoA”) uplatnenie v mnohých odvetviach, napríklad na vojenské účely, pri záchranných a pátracích akciách, na ochranu verejnosti a v neposlednom rade v bezdrôtových sieťach. V posledných desaťročiach navyše došlo k revolúcii v oblasti bezdrôtových komunikácií. O jej veľký podiel sa zaslúžil vývoj inteligentných antén. Tieto antény využívajú metódy odhadu DoA spolu s technikami na riadenie anténneho zväzku na implementáciu sledovacích mechanizmov, ktoré umožňujú zvýšenie prenosových rýchlostí a potlačenie rušenia od ostatných užívateľov. V posledných rokoch sa technológia inteligentných antén začala nachádzať uplatnenie aj vo vesmírnom priemysle. Antény sa využívajú nielen na satelitoch, ale aj na pozemných staniciach a efektívne navyšujú komunikačné aj navigačné schopnosti. Toto využitie slúžilo ako hlavná motivácia tejto diplomovej práce, ktorej cieľom je vyvinúť demonštračnú platformu na implementáciu techník odhadu DoA na cenovo dostupnom hardvéri s cieľom potenciálnej budúcej adaptácie v modernom systéme inteligentných antén pre satelitnú komunikáciu.

V prvej kapitole sú popísané základné princípy príjmu signálov anténou radou, ktoré sú kľúčové pre pochopenie obsahu nasledovných kapitol. Druhá kapitola popisuje populárne metódy pre odhad DoA rozdelené do kategórií metód založených na báze tvarovania zväzku, na báze podpriestorov a na báze metód maximálnej pravdepodobnosti. Opísané sú aj techniky pre predspracovanie signálu, ktoré preukázateľne zvyšujú efektivitu niektorých popísaných metód. Tretia kapitola predstavuje stručný úvod do hardvéru softvérovo-definovaných rádií (SDR). Tieto prvé kapitoly môžu poslúžiť ako úvod pre začiatočníkov v oblasti odhadu DoA. V štvrtej kapitole je vykonaný prieskum trhu dostupných platforiem SDR, pričom sú posúdené rozdiely medzi komerčne dostupnými a na mieru prispôbenými hardvérovými riešeniami. Bola vybraná optimálna SDR platforma, pre ktorú sa navrhli kompletné hardvérové a softvérové riešenia pre implementáciu a overenie algoritmov pre odhad DoA. V piatej kapitole boli algoritmy implementované pomocou simulácií spolu so simuláciami anténneho poľa, s cieľom posúdiť efektivitu algoritmov a vplyv zmien parametrov anténnej rady na zjednodušenom modeli. Posledná kapitola bola zameraná na návrh a vykonanie experimentálnych meraní slúžiacich na overenie správnej implementácie algoritmov pre odhad DoA pomocou navrhnutého hardvéru. Výsledky merania boli nakoniec kriticky zhodnotené.

Výsledky prvého merania preukázali funkčnosť algoritmov pre jednoduchý prípad príchodu jedného signálu z malých uhlov od stredu anténnej rady. Druhé meranie

preukázalo znížené rozlišovacie schopnosti pri nižších hodnotách pomeru signálu k šumu. Výsledky posledného merania v porovnaní so simuláciami indikujú značne obmedzenú schopnosť algoritmov rozlíšiť dva koherentné zdroje umiestnené blízko pri sebe. Značný rozdiel mohol byť spôsobený využitím iba jedného generátora signálu pre obe antény, predstavujúce nezávislé zdroje. Koherencia medzi signálmi mohla byť tak násobne vyššia ako je bežné v reálnych podmienkach. Navyše sa zistilo, že absorbéry v bezodrazovej komore majú pomerne vysoký činiteľ odrazu. To pravdepodobne značne prispelo k viaccestnému šíreniu signálov odrazmi od stien komory, čo znižovalo celkovú presnosť meraní. Prítomnosť dodatočných signálov z viaccestného šírenia môže byť preukázaná aj zlyhaním predspracovacej metódy priemerovania napred-vzad (FBA). Tá je účinná len v prípade prítomnosti dvoch signálov, inak sa stáva neúčinnou.

# Author's Declaration

**Author:** Bc. David Sedláček  
**Author's ID:** 221347  
**Paper type:** Master's Thesis  
**Academic year:** 2023/24  
**Topic:** Software-defined antenna array

I declare that I have written this paper independently, under the guidance of the advisor and using exclusively the technical references and other sources of information cited in the paper and listed in the comprehensive bibliography at the end of the paper.

As the author, I furthermore declare that, with respect to the creation of this paper, I have not infringed any copyright or violated anyone's personal and/or ownership rights. In this context, I am fully aware of the consequences of breaking Regulation § 11 of the Copyright Act No. 121/2000 Coll. of the Czech Republic, as amended, and of any breach of rights related to intellectual property or introduced within amendments to relevant Acts such as the Intellectual Property Act or the Criminal Code, Act No. 40/2009 Coll. of the Czech Republic, Section 2, Head VI, Part 4.

Brno .....  
.....  
author's signature\*

---

\*The author signs only in the printed version.



## ACKNOWLEDGEMENT

I would like to thank my thesis advisor, prof. Ing. Roman Maršálek, Ph.D., for their wise advice, willingness, and courtesy.

I would also like to thank my consultant, Ing. Jan Vélím, along with the rest of the RF engineering team at Groundcom.space, including Ing. Miroslav Cupal, Ph.D., and Ing. Michal Mrnka, Ph.D., for their excellent communication, dedication, and kind-hearted encouragement.

# Contents

<b>Introduction</b>	<b>15</b>
<b>1 Phased antenna arrays</b>	<b>16</b>
1.1 Array fundamentals . . . . .	16
1.2 Array parameters . . . . .	18
1.3 Model simplifications . . . . .	20
1.4 Uniform linear arrays . . . . .	21
1.5 Uniform circular arrays . . . . .	23
<b>2 Direction-of-Arrival estimation</b>	<b>26</b>
2.1 Covariance matrix . . . . .	26
2.2 Beamforming techniques . . . . .	27
2.2.1 Bartlett's beamformer . . . . .	28
2.2.2 MVDR . . . . .	29
2.2.3 Linear prediction . . . . .	29
2.3 Subspace-based techniques . . . . .	30
2.3.1 MUSIC . . . . .	31
2.3.2 Root-MUSIC . . . . .	33
2.3.3 Min-norm MUSIC . . . . .	34
2.4 Maximum likelihood techniques . . . . .	34
2.5 Signal preprocessing techniques . . . . .	35
2.5.1 Forward-backward averaging (FBA) . . . . .	36
2.5.2 Spatial smoothing . . . . .	36
2.6 Model order estimation . . . . .	38
2.6.1 Minimum descriptive length criterion . . . . .	39
<b>3 Software-defined radio</b>	<b>40</b>
3.1 RF architectures . . . . .	41
3.2 Requirements for DoA estimation . . . . .	42
<b>4 Hardware &amp; software setup</b>	<b>44</b>
4.1 Market research . . . . .	44
4.1.1 Chosen SDR platform . . . . .	49
4.2 KrakenSDR setup . . . . .	51
4.2.1 Hardware solution . . . . .	51
4.2.2 Software solution . . . . .	53

<b>5</b>	<b>Array and DoA estimation performance analysis</b>	<b>56</b>
5.1	Array pattern analysis . . . . .	56
5.2	DoA estimation performance for ULA . . . . .	59
5.3	DoA estimation performance for UCA . . . . .	65
<b>6</b>	<b>Practical verification of DoA estimation methods</b>	<b>67</b>
6.1	Proposed measurement setup . . . . .	67
6.2	DoA estimation measurements . . . . .	69
6.2.1	Verification of functionality . . . . .	70
6.2.2	DoA estimation in low SNR environment . . . . .	72
6.2.3	DoA estimation of two coherent signals . . . . .	72
	<b>Conclusion</b>	<b>77</b>
	<b>Bibliography</b>	<b>79</b>
	<b>Symbols and abbreviations</b>	<b>82</b>

# List of Figures

1.1	An exemplar antenna array. . . . .	17
1.2	Illustration of signal paths and element spacing using Pythagorean theorem. . . . .	17
1.3	Propagation of the planar wave impinging the array. . . . .	21
1.4	Propagation of the planar wave impinging the UCA. . . . .	23
1.5	Propagation of the planar wave impinging the UCA extended to three-dimensional space. . . . .	24
2.1	Sub-array division of ULA for forward and backward spatial smoothing. . . . .	37
3.1	Block diagram of a general communication system. . . . .	40
4.1	KrakenSDR with 5 monopole whip antennas. . . . .	51
4.2	Presented KrakenSDR configurations. . . . .	52
4.3	GNU Radio block diagram for recording of IQ samples. . . . .	54
5.1	Normalised ULA pattern based on the number of array's elements. . . . .	56
5.2	Normalised ULA pattern based on the scan angle. . . . .	57
5.3	Normalised ULA pattern based on increasing inter-element distance. . . . .	58
5.4	Normalised ULA pattern of based on decreasing inter-element distance. . . . .	58
5.5	Normalised ULA pattern with spatial tapering using windowing functions. . . . .	59
5.6	Spatial spectra of DoA estimation techniques for $\theta_1 = 10^\circ$ and $\theta_2 = 40^\circ$ . . . . .	61
5.7	RMSE of DoA estimation techniques based on $\Delta\theta$ . . . . .	61
5.8	RMSE of DoA estimation techniques based on SNR. . . . .	62
5.9	Spatial spectra of DoA estimation techniques in the presence of two highly coherent signals. . . . .	63
5.10	Spatial spectra of Beamforming DoA estimation techniques in the presence of two highly coherent signals with no noise present. . . . .	63
5.11	Effects of preprocessing methods on DoA estimation techniques with decreasing SNR. . . . .	64
5.12	Spatial spectra of DoA estimation techniques for UCA configuration. . . . .	66
5.13	RMSE of DoA estimation techniques based on SNR for UCA configuration. . . . .	66
6.1	Proposed measurement setup . . . . .	69
6.2	Image of the deployed setup in the anechoic chamber. . . . .	70
6.3	Resulting spatial spectra of beamforming methods applied on recorded data sample. . . . .	71
6.4	Resulting spatial spectra of subspace-based methods applied on recorded data sample. . . . .	71

6.5	RMSE of estimation techniques for the decreasing amplitude of the generated signal impinging on the array from $0^\circ$ s. . . . .	73
6.6	RMSE of estimation techniques for the decreasing amplitude of the generated signal impinging on the array from $45^\circ$ s. . . . .	73
6.7	RMSE of estimation techniques based on the angle between two coherent sources. . . . .	74
6.8	RMSE of estimation techniques with FBA based on the angle between two coherent sources. . . . .	75
6.9	RMSE of estimation techniques with FB-SS based on the angle between two coherent sources. . . . .	75
6.10	MUSIC spectrum for two coherent sources with 15 degree angular distance. . . . .	76

# List of Tables

4.1	Frequency ranges of the most popular tuners. . . . .	47
4.2	Overview of all important parameters of considered SDRs. . . . .	50
5.1	Approximate code execution times for various DoA estimation techniques. . . . .	65
6.1	Anechoic chamber parameters. . . . .	67
6.2	KrakenSDR configuration for the first experiment. . . . .	69
6.3	Performance measurements based on absolute deviation of estimation algorithms. . . . .	72
6.4	Signal source angles along with required shifts in source positions. . .	74

# Introduction

The beginnings of estimation of directions of incoming signals can be tracked back to early experiments aimed at determining the position of cellular devices during emergency calls. Since then, the estimation of the direction of radio frequency (RF) signals has found applications in a wide range of fields. These include military applications, public security, search and rescue, and wireless networking.

Over the past few decades, the development of smart antenna technology [1] has revolutionised the field of wireless communications. Smart antennas use the direction-of-arrival (DoA) estimation alongside electronic beam steering techniques, implementing tracking mechanisms, enabling higher information throughput, while reducing interference with other users. In recent years, there has been growing interest in the implementation of smart antennas for space-borne applications, where they are utilised both onboard satellites and at ground stations to improve communication and navigation capabilities. This has also been the main motivation behind this thesis, which aims to develop a demonstration platform for implementing DoA estimation techniques on cost-efficient hardware, with the goal of potential future adaptation in a modern smart antenna system for satellite communications.

The work begins with an introduction to phased arrays, providing insight into the physical principles of signals impinging on array structures crucial for understanding topics discussed in later chapters. This is followed by an in-depth examination of DoA estimation theory, explaining the mechanisms of beamforming, subspace-based and maximum likelihood estimation techniques. This chapter also includes a description of signal preprocessing techniques, which have been proven to enhance the estimation capabilities of proposed DoA estimation algorithms. Next, a brief introduction to the software-defined radio (SDR) hardware is provided. These sections may serve as introductory material for researchers and developers new to the field. A subsequent analysis of available SDR platforms is performed, assessing the trade-offs between commercially available hardware and custom solutions for DoA estimation. Suitable hardware is chosen, and the appropriate setup is proposed for implementation and validation of processing algorithms. Following this, the performance of proposed DoA estimation algorithms, along with effects of array configuration on the array radiation pattern, is analysed through software simulations. Finally, a testbed is proposed to evaluate the performance of the developed algorithms implemented on the selected hardware. Measurements are conducted, and the results are critically evaluated.

# 1 Phased antenna arrays

Phased antenna arrays electronically steer (or “scan”) the antenna beam to a desired direction without the need of using any mechanical components, as compared to mechanically scanned arrays. Consequently, they are often referred to as electronically scanned arrays (ESAs). They are often found at the transmitting or receiving ends of a communication link, where their design allows for directional beamforming and specialised signal processing. Phased arrays can be categorised into three types based on their operational principles [2]:

- **Passive electronically scanned arrays (PESAs):** In PESAs, signals received by individual array elements are phase shifted through analog phase shifters before being combined and amplified by a common low-noise amplifier (LNA). The signal processing chain following the LNA is unified, leading to a simple but power-inefficient setup. The positioning of the LNA further down the signal path results in significant power loss. Furthermore, the failure of any component in the unified front-end renders the entire system inoperable. PESAs played a significant role in early radar years as they allowed for much higher scanning speeds compared to MSAs. However, over time, they have been surpassed by more sophisticated alternatives.
- **Active electronically scanned arrays (AESAs):** AESAs overcome limitations of PESAs by employing a separate front-end for each individual antenna element with its own LNA. This not only minimises power losses as the amplification happens early in the analog chain but also improves the system’s reliability, as no failure of a singular front-end leads to the system’s inoperability. Initially, the complexity of AESAs made them expensive and challenging to manufacture. It was only the breakthrough in GaAs semiconductor technologies, which contributed to their predominance in modern radar applications.
- **Hybrid arrays:** In hybrid arrays, elements are grouped into multiple sub-arrays individually resembling PESAs, yet each group is equipped with a separate RF front-end just like in AESAs. Hybrid arrays are gaining popularity, as they offer a great balance between efficiency, reliability, and cost. Hybrid array architecture is also employed by Starlink’s user terminal.

## 1.1 Array fundamentals

Antenna array is a collection of antennas working in unison to transmit or receive signals over an electromagnetic medium. A singular isolated antenna of the array is referred to as an array element. By introducing a fixed or variable phase delay on



the elements, the radiation pattern can be rotated and reshaped to adapt to varying conditions in the environment. This can be done both in hardware and software. At the receiving end, signals received by array's elements are either synchronised and analysed separately or combined and further processed for various applications. An exemplar array is shown on Figure 1.1, with its elements distributed uniformly in a line.

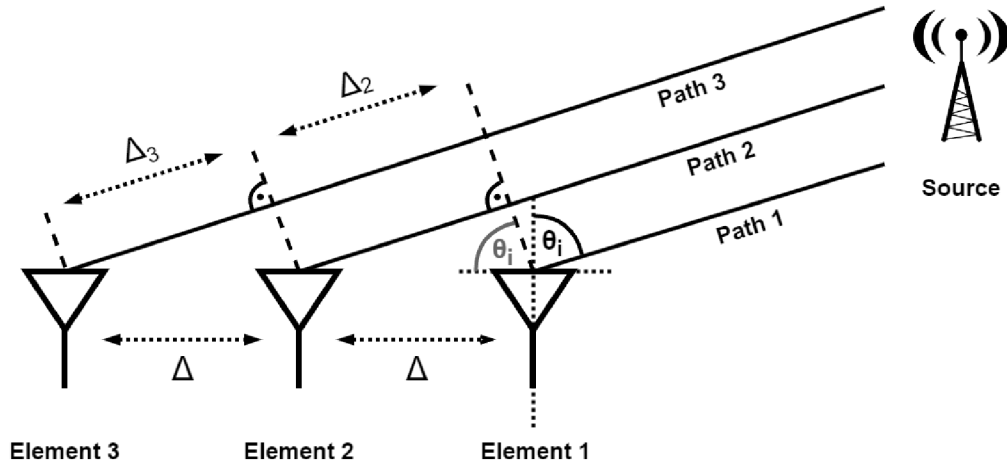


Fig. 1.1: An exemplar antenna array.

Angle  $\theta_i$  is the angle of incidence and is measured between the antenna boresight and the direction of the signal and  $\Delta$  is the distance between two adjacent elements. A signal is generated from a source located at a distance much greater compared to array's own dimensions. All the signal paths can thus be approximated as parallel to each other and the distance between adjacent elements can be determined using Pythagorean theorem as shown in Figure 1.2.

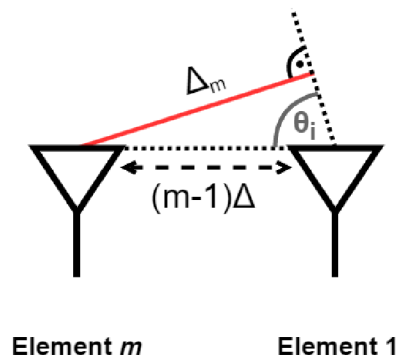


Fig. 1.2: Illustration of signal paths and element spacing using Pythagorean theorem.

Having the 1st element set as a reference, the distance to any other element can

be obtained, as:

$$\Delta_m = (m - 1)\Delta \sin(\theta_i)$$

In this example,  $m = 1, 2, 3$ . Ignoring any noise and non-linearities, the signals on individual array elements are:

$$\begin{aligned} s_1^{rx}(t) &= s(t) \\ s_2^{rx}(t) &= s(t)e^{-j\beta\Delta_2} = s(t)e^{-j2\pi\Delta/\lambda \sin(\theta_i)} \\ s_3^{rx}(t) &= s(t)e^{-j\beta\Delta_3} = s(t)e^{-j2\pi2\Delta/\lambda \sin(\theta_i)} \end{aligned}$$

The signal must travel the added distance to reach the other elements. That results in a phase shift, which is defined by a phase constant  $\beta = 2\pi/\lambda$  and the distance  $\Delta_m$ .  $\lambda$  is the signal's wavelength. In the matrix form, the signals may be then defined as follows:

$$s^{rx}(t) = \begin{bmatrix} 1 \\ e^{-j2\pi\Delta/\lambda \sin(\theta_i)} \\ e^{-j2\pi2\Delta/\lambda \sin(\theta_i)} \end{bmatrix} s(t) = \begin{bmatrix} 1 \\ e^{j\mu} \\ e^{j2\mu} \end{bmatrix} s(t) = a(\mu)s(t) \quad (1.1)$$

Here,  $\mu = -2\pi\Delta/\lambda \sin(\theta_i)$  is called the spatial frequency and  $a(\mu) = [1 \ e^{j\mu} \ e^{j2\mu}]^T$  is often denoted as the array steering vector.

The equation can be generalised as:

$$s^{rx}(t) = \begin{bmatrix} 1 \\ e^{-j2\pi\Delta/\lambda \sin(\theta_i)} \\ \vdots \\ e^{-j(M-1)2\pi\Delta/\lambda \sin(\theta_i)} \end{bmatrix} s(t) = \begin{bmatrix} 1 \\ e^{j\mu} \\ \vdots \\ e^{j(M-1)\mu} \end{bmatrix} s(t) = a(\mu)s(t) \quad (1.2)$$

It is important to note that any element can be thought of as a reference element, but the array steering vector must be adjusted to the change in phase shift relations. In addition, the equation is limited only to signals on uniformly distributed  $M$ -element linear arrays. By modifying the array steering vector  $a(\mu)$ , one can define signals on an arbitrary array, allowing for analysis of much more complex array geometries.

## 1.2 Array parameters

Array parameters can effectively describe the performance of an array by detailing the characteristics of its individual elements. A standardised list of antenna parameters is provided in [3]. However, these parameters are often interrelated, and not all are necessary to sufficiently capture the antenna's performance in relation to its use case. [4] [5] describe the core metrics used in modern antenna analysis and design practices. A handful of the most important parameters often investigated for DoA estimation applications are:

- **Antenna pattern or radiation pattern** defines directional properties of an antenna. It defines two-dimensional or three-dimensional spatial distribution of radiated energy at a constant radius around the antenna, represented by a mathematical function, which can be further graphically visualised. When the function describes the electric and magnetic fields excited by the antenna, the pattern is referred to as a “field pattern”. Else, when the function is based on the radiation intensity, which denotes the distance normalised power density (useful when describing far-field radiation patterns), the pattern is called the “power pattern”. The radiation pattern of an antenna array can achieve various shapes based not only on properties of individual elements but also on their spatial configuration within the array.
- **Radiation pattern lobes** are portions of the radiation pattern bounded by areas of relatively weak radiation intensity. They form due to the non-isotropic properties of the antenna. The lobe that forms in the direction of maximum radiation is called the “main lobe”, while those formed in unintended directions are referred to as “side lobes”. Many array configurations enable pattern formations that facilitate spatial filtering of incoming signals, forming useful lobes in the directions of useful signals.
- **Beamwidth** typically defines the width of the main lobe measured at two points on either side of the maximum, where the radiation intensity drops to half-power (-3 dB), commonly referred to as Half-Power Beam Width (HPBW). The width of side lobes is determined similarly, with the maximum being that of the side lobe under investigation. A general formula for calculation of HPBW for a broadside ULA is defined as:

$$\Theta_{\text{HPBW}} \approx 2 \left[ \frac{\pi}{2} - \cos^{-1} \left( \frac{1.391\lambda}{\pi Nd} \right) \right] \quad (1.3)$$

where  $\lambda$  is the wavelength,  $N$  is the number of elements and  $d$  is the inter-element distance.

[4] limits the equation to cases where  $\pi d/\lambda \ll 1$ . Nevertheless, it can serve as a rough estimate even for general cases, where the condition is not strictly met.

- **Antenna field regions** define boundaries where changes in the behaviour of electromagnetic fields can be expected. These regions originate from the fact that not all generated electromagnetic fields radiate into space. Although no immediate changes are noticeable after crossing the field boundaries, each region can be characterised by its own distinct properties. Conventionally, these regions are defined as follows:
  - **Reactive near-field region:** This region is dominated by the reactive field, which stores energy similarly to how capacitors and inductors store

energy in a lumped circuit. This region forms at a distance  $R \leq 0.62\sqrt{\frac{D^3}{\lambda}}$ , where  $D$  is the maximum overall dimension of the antenna.

- **Radiating near-field region (Fresnel region):** Dominated by the radiating field, the energy in this region radiates into space, but the electric and magnetic field components diminish at different rates. This variability results in a changing radiation pattern relative to distance. The region forms at distance  $0.62\sqrt{\frac{D^3}{\lambda}} \leq R \leq \frac{2D^2}{\lambda}$ . In theory, if  $D$  is much smaller than  $\lambda$ , this region may not form.
- **Far-field region (Fraunhofer region):** In this region, the radiation pattern stops changing with distance. Most commonly the far-field region is expected at distances  $\frac{2D^2}{\lambda} \leq R$ .

### 1.3 Model simplifications

Modern digital signal processing (DSP) studies rely on model-based representation of real-world conditions. Specific assumptions are made, under which concepts of beamforming and signal processing can be demonstrated and understood. The following assumptions are maintained throughout the entire thesis:

- **Far-field region:** Signal sources are located in the far-field region of an array. The electromagnetic wave arriving at the elements can be considered as planar. Signal received by individual elements thus comes from an equal direction and paths are assumed to be parallel to each other.
- **Linear and isotropic medium:** The transmission medium between sources and arrays has the same physical properties in all directions and at any point in space waves can be combined by the principle of superposition.
- **Narrow-band signals:** Signals generated by sources have a carrier frequency  $f_c$ . Any of these signals can thus be mathematically expressed as:

$$s_i^{\text{tx}}(t) = \alpha_i(t) \cos(2\pi f_c t + \beta_i(t)) = \text{Re}\{\alpha_i(t)e^{j(2\pi f_c t + \beta_i(t))}\} \quad (1.4)$$

For such a signal to be considered narrow-band, the change in amplitude  $\alpha_i(t)$  and the phase  $\beta_i(t)$  must be insignificant compared to the time it takes the signal to travel from one element to the next, often denoted as  $\tau$ . This is ensured if the frequency components are concentrated in a close vicinity of the carrier.

- **AWGN channel:** Each received signal includes an additive, zero-mean, white Gaussian noise with variance  $\sigma_N^2$ . It is a spatially uncorrelated spatial random process, uncorrelated with the signals. Hence, the noise must also be uncorrelated at the receiver's output, which is an essential concept in many DSP applications.

## 1.4 Uniform linear arrays

Uniform Linear Array (ULA) [6] forms the simplest geometry, where the elements are arranged in a straight line. A simple 3-element ULA was roughly outlined in 1.1. The scenario can now be generalised. An  $i$ -th source is generating signal  $s_i^{tx}(t)$ , which is impinging the array as shown in Figure 1.3.

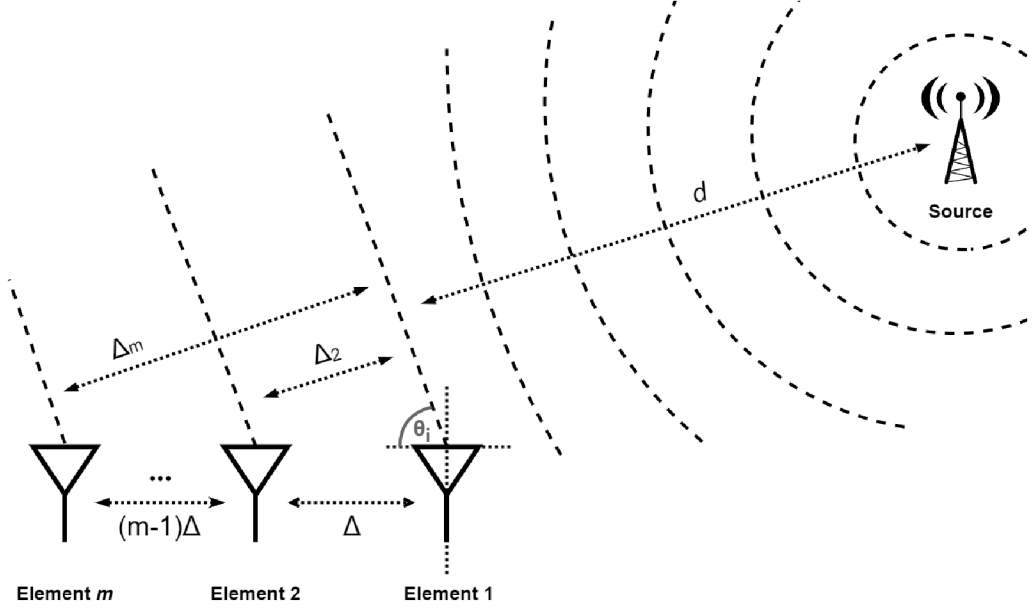


Fig. 1.3: Propagation of the planar wave impinging the array.

Here,  $d$  is the distance between the source and the reference element,  $\theta_i$  is an angle of incidence,  $\Delta$  is the distance between the neighbouring array elements, and  $\Delta_m$  is the distance between the  $m$ -th element and the reference. Let the rightmost element be the reference. As the electromagnetic wave propagating through space travels at the speed of light  $c$ , the signal  $s_{i1}(t)$  at this element is a delayed copy of  $s_i^{tx}(t)$ , delayed by  $\tau_d = \frac{d}{c}$ . Therefore,

$$s_{i1}(t) = s_i^{tx}(t - \tau_d) = \Re\{\alpha_i(t)e^{j(2\pi f_c(t-\tau_d)+\beta_i(t-\tau_d))}\} \quad (1.5)$$

The added delay between the first and an  $m$ -th element is:

$$\tau_m = \frac{\Delta_m}{c} = \frac{(m-1)\Delta \sin(\theta_i)}{c} \quad (1.6)$$

Where  $\Delta_m$  is the distance the signal takes travelling to the  $m$ -th element. Signal on the  $m$ -th element can then be interpreted as a delayed version of the signal from the source:

$$\begin{aligned} s_{im}(t) &= s_{i1}(t - \tau_m) = s_i(t - \tau_d - \tau_m) \\ &= \alpha_i(t - \tau_d - \tau_m) \cos(2\pi f_c(t - \tau_d - \tau_m) + \beta_i(t - \tau_d - \tau_m)) \end{aligned} \quad (1.7)$$

Applying the narrow-band assumptions:

$$\begin{aligned}
s_{im}(t) &\approx \alpha_i(t - \tau_d) \cos(2\pi f_c(t - \tau_d) + \beta_i(t - \tau_d) - 2\pi f_c \tau_m) \\
&= \alpha_i(t - \tau_d) \cos((2\pi f_c(t - \tau_d) + \beta_i(t - \tau_d) - (m - 1)\mu_i) \\
&= \Re\{s_{i1}(t)e^{j(m-1)\mu_i}\} \quad (1.8)
\end{aligned}$$

$\mu_i$  is the spatial frequency associated with the  $i$ -th signal source. In the modelled environment that approximates real-world conditions, signals are superposed together with noise. To differentiate between signals generated by  $N$  sources and received noise-corrupted signals, the signal received by an  $m$ -th element is often called “data” and is denoted as:

$$x_m(t) = \sum_{i=1}^N s_{im}(t) + n_m(t) = s_{i1}(t) \sum_{i=1}^N e^{j(m-1)\mu_i} + n_m(t) \quad (1.9)$$

Hence, the resulting signal at the array’s output can be described in a matrix form:

$$\mathbf{x}(t) = \begin{bmatrix} a(\mu_1) & a(\mu_2) & \cdots & a(\mu_N) \end{bmatrix} \begin{bmatrix} s_1^x(t) \\ s_2^x(t) \\ \vdots \\ s_N^x(t) \end{bmatrix} + \begin{bmatrix} n_1(t) \\ n_2(t) \\ \vdots \\ n_N(t) \end{bmatrix} = \mathbf{A}\mathbf{s}(t) + \mathbf{n}(t) \quad (1.10)$$

where  $\mathbf{x}(t)$  is the data column vector,  $\mathbf{s}(t)$  the signal column vector,  $\mathbf{n}(t)$  is an additive white Gaussian noise vector, and  $\mathbf{A}$  is a  $m \times N$  array steering matrix, defined as:

$$\mathbf{A} = \begin{bmatrix} 1 & 1 & \cdots & 1 \\ e^{j\mu_1} & e^{j\mu_2} & \cdots & e^{j\mu_N} \\ \vdots & \vdots & \ddots & \vdots \\ e^{j(m-1)\mu_1} & e^{j(m-1)\mu_2} & \cdots & e^{j(m-1)\mu_N} \end{bmatrix} \quad (1.11)$$

Where  $m$  is the number of elements in the array and  $N$  is the amount of signal sources. Columns of this matrix are formed by array steering vectors corresponding to the directions of arrival of individual signals in the signal column vector. Matrix  $A$  is then a Vandermonde matrix which reduces the complexity of matrix operations.

The ULA enables straightforward application of beamforming and signal processing algorithms, but its simplicity comes with significant drawbacks. The primary issue is the 180-degree ambiguity. The array pattern is symmetrical around the element axis, making it impossible to distinguish whether the signal impinges the array from the front or the back. Consequently, the scanning range is restricted from  $-90$  to  $90$  degrees from the perspective of array boresight. Moreover, the effective length of the array decreases when approaching the array’s end-fire directions. This directly increases the beamwidth of the main lobe when steered in such directions.

In practice, the usable scanning range of ULAs is limited to  $-60$  to  $60$  degrees. The limited range can be overcome by employing multiple ULAs in configurations that ensure broader spatial coverage.

## 1.5 Uniform circular arrays

A Uniform Circular Array (UCA) [5][7] consists of elements equally distributed along a circular ring. This configuration can be beneficial in situations where size restrictions do not allow for ULA configuration. An  $M$ -element UCA is impinged by a signal  $s_i^{tx}(t)$  generated by the  $i$ -th source arriving from an arbitrary direction as shown in Figure 1.4.

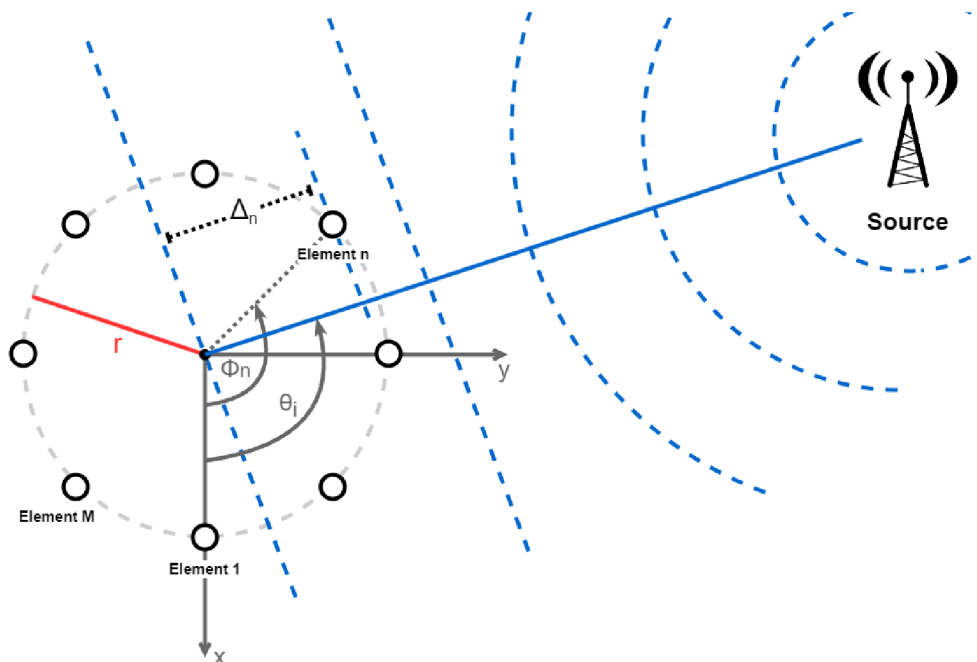


Fig. 1.4: Propagation of the planar wave impinging the UCA.

Here,  $r$  is the radius of the ring,  $\theta_i$  is the angle of incidence,  $\phi_n = \frac{2\pi}{M}(n - 1)$  is the angular position of the  $n$ -th element related to the first element, and  $\Delta_n$  is the distance from the origin to the  $n$ -th element measured from the perspective of a planar wavefront. Let the origin be the reference. The signal  $s_{i0}(t)$  at the origin is a delayed copy of  $s_i^{tx}(t)$ , as expressed in equation 1.5. The wavefront passes through the origin at time  $t = 0$  seconds. The distance  $\Delta_n$  can be then obtained as:

$$\Delta_n = -r \cdot \cos(\theta_i - \Phi_n) \quad (1.12)$$

The minus sign in the equation correctly reflects the distance in relation to the wavefront at the origin. The delay on the  $n$ -th element is:

$$\tau_n = \frac{\Delta_n}{c} = -\frac{r}{c} \cos(\theta_i - \Phi_m) \quad (1.13)$$

If the resulting time delay is negative, the wavefront arrives at the  $n$ -th element before passing through the origin. The data on this element is then denoted by:

$$x_m(t) = s_{io}(t) \sum_{i=1}^N e^{-j\frac{2\pi r}{\lambda} \cos(\theta_i - \Phi_m)} + n_m(t) \quad (1.14)$$

The array steering vector can be written as:

$$\mathbf{a}(\theta_i) = \left[ e^{-j\frac{2\pi r}{\lambda} \cos(\theta_i - \Phi_1)}, \dots, e^{-j\frac{2\pi r}{\lambda} \cos(\theta_i - \Phi_M)} \right]^T \quad (1.15)$$

So far, impinging signals were considered only in terms of their arrival from arbitrary directions within the azimuth plane. However, the two-dimensional configuration of UCA allows for the determination of incoming directions in three-dimensional space as well. Consider a scenario depicted in Figure 1.5, where an arriving wavefront of a signal  $s_i^{tx}(t)$  generated by the  $i$ -th source is represented in a spherical coordinate system.

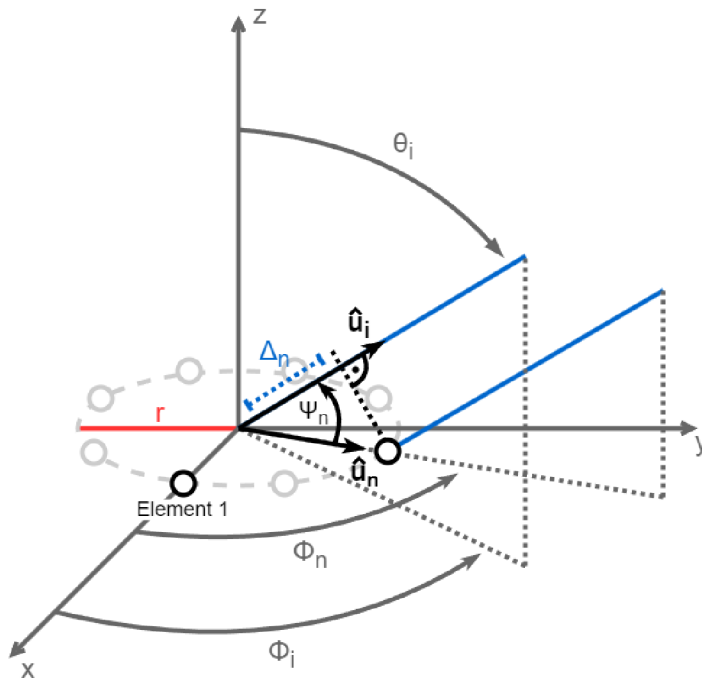


Fig. 1.5: Propagation of the planar wave impinging the UCA extended to three-dimensional space.

The planar wave impinging the array is denoted by elevation  $\theta_i$  and azimuth  $\phi_i$ . The unit vector  $\hat{u}_i$  from the origin perpendicular to the planar wave can be



represented in Cartesian coordinates as:

$$\hat{u}_i = \hat{u}_x \sin(\theta_i) \cos(\phi_i) + \hat{u}_y \sin(\theta_i) \sin(\phi_i) + \hat{u}_z \cos(\theta_i) \quad (1.16)$$

The unit vector from the origin to the  $n$ -th element is given by:

$$\hat{u}_n = \hat{u}_x \sin(\phi_n) \cos(\phi_n) + \hat{u}_y \sin(\phi_n) \sin(\phi_n) \quad (1.17)$$

The distance  $\Delta_n$  is obtained as:

$$\Delta_n = -|\Delta \vec{n}| = -|\hat{u}_i r \cos(\psi_n)| = |\hat{u}_i r (\hat{u}_i \cdot \hat{u}_n)| = -r \sin(\theta_i) \cos(\phi_i - \phi_n) \quad (1.18)$$

The delay at the  $n$ -th element can be then expressed as:

$$\tau_n = \frac{\Delta_n}{c} = -\frac{r}{c} \sin(\theta_i) \cos(\phi_i - \phi_n) \quad (1.19)$$

Hence, the resulting data signal will take the form:

$$x_m(t) = s_{io}(t) \sum_{i=1}^N e^{-j \frac{2\pi r}{\lambda} \sin(\theta_i) \cos(\phi_i - \phi_n)} + n_m(t) \quad (1.20)$$

The output data matrix for  $N$ -signal sources will take on the same form as for ULA in 1.10, with the exception of the array steering matrix  $\mathbf{A}$ , where

$$\mathbf{A} = \begin{bmatrix} e^{-j \frac{2\pi r}{\lambda} \sin(\theta_1) \cos(\phi_1 - \phi_1)} & \dots & e^{-j \frac{2\pi r}{\lambda} \sin(\theta_N) \cos(\phi_N - \phi_1)} \\ e^{-j \frac{2\pi r}{\lambda} \sin(\theta_1) \cos(\phi_1 - \phi_2)} & \dots & e^{-j \frac{2\pi r}{\lambda} \sin(\theta_N) \cos(\phi_N - \phi_2)} \\ \vdots & \ddots & \vdots \\ e^{-j \frac{2\pi r}{\lambda} \sin(\theta_1) \cos(\phi_1 - \phi_M)} & \dots & e^{-j \frac{2\pi r}{\lambda} \sin(\theta_N) \cos(\phi_N - \phi_M)} \end{bmatrix} \quad (1.21)$$

The main advantages of UCAs in comparison to ULAs are the extended scanning coverage up to 360 degrees in the azimuth plane and the ability to extend the scanning range to three-dimensional space. On the other hand, the non-uniform element spacing relative to the direction of the impinging signal affects the size and distribution of side lobes, which in turn impacts the array's resolution capability. Moreover, this configuration is more sensitive to mutual coupling between the elements of the array and to inaccuracies in element positioning, both of which may further reduce the array's performance. Lastly, the non-Vandermonde structure of matrix  $A$  increases the complexity of signal processing computations. Despite these limitations, UCAs have been used extensively in applications, where a wide scanning range is essential and a reduction in accuracy is an acceptable trade-off.

## 2 Direction-of-Arrival estimation

Various techniques are employed to estimate the Direction of Arrival (DoA) of signals within a specified region of interest surrounding the array. The objective of these techniques is to devise an estimation scheme that strongly correlates with the actual direction of the incoming signals. The fundamental concept underlying this correlation is the utilisation of the array's degrees of freedom. In the context of phased arrays, the term "degrees of freedom" essentially refers to the number of parameters that can be independently manipulated to enhance the array's ability to accurately determine the direction of incoming signals. They often correspond to the array's elements.

DoA estimation techniques can be divided into three distinct categories:

- Beamforming methods
- Space-based methods
- Maximum likelihood methods

Some methods may lose resolution or completely fail in the presence of multiple correlated signals. Therefore, preprocessing methods are often applied before DoA estimation, along with methods for estimating the number of sources. The significance of additional processing will be described in more detail in the relevant sections. Estimations are conducted within a discrete space domain, in which the area of investigation around the array is divided into  $M$  directional samples. Increasing the sample count enhances the precision of the estimation. However, higher precision can only be achieved at the expense of increased computational time.

### 2.1 Covariance matrix

As demonstrated in 1.4, received signals are corrupted by noise present in the transmission medium, which may impair the estimation results if not dealt with correctly. According to the foundational assumptions outlined in 1.3, the noise within the system is presumed to be uncorrelated. Conversely, the unaltered components of the received signals, essentially phase-shifted replicas of their original signals, are expected to display a significant correlation when subjected to analysis. This relationship can be quantitatively assessed through the covariance matrix:

$$\mathbf{R}_{\mathbf{xx}} = \mathbb{E}\{\mathbf{x}(t)\mathbf{x}^H(t)\} \quad (2.1)$$

where  $\mathbb{E}\{\}$  indicates the statistical expectation, representing the weighted average of all possible outcomes of a random variable, weighted by their probability of occurrence, assuming its distribution is fully known.

Substituting 1.10 into 2.1:

$$\mathbf{R}_{\mathbf{xx}} = \mathbf{A}E\{\mathbf{s}(t)\mathbf{s}^H(t)\}\mathbf{A}^H + E\{\mathbf{n}(t)\mathbf{n}^H(t)\} = \mathbf{A}\mathbf{R}_{\mathbf{ss}}\mathbf{A}^H + \sigma_N^2\mathbf{I}_m \quad (2.2)$$

where  $\mathbf{R}_{\mathbf{ss}}$  is the pure signal covariance matrix and  $\mathbf{I}_m$  is an identity matrix.

In Digital Signal Processing (DSP), direct calculation of this matrix is impractical, as the available data is sampled over a finite interval. By assuming that all the noise processes are ergodic, ensemble averages can be substituted by time averages. The distribution can be approximated from the available discrete sample sets of  $\mathbf{x}(t)$ . The data is represented by discrete samples taken at time intervals determined by the sampling period, which is set to fulfil the criteria established by the Nyquist-Shannon theorem [8], to ensure accurate digital representation. Let  $\mathbf{X}$  denote the data matrix composed of  $K$  samples:

$$\begin{aligned} \mathbf{X} &= \begin{bmatrix} x(t_1) & x(t_2) & \cdots & x(t_K) \end{bmatrix}^T \\ &= \mathbf{A} \cdot \begin{bmatrix} s(t_1) & s(t_2) & \cdots & s(t_K) \end{bmatrix}^T + \begin{bmatrix} n(t_1) & n(t_2) & \cdots & n(t_K) \end{bmatrix}^T \end{aligned} \quad (2.3)$$

The data here represents a sequence of time samples of data matrix from 1.10. The data covariance matrix time average estimate  $\hat{\mathbf{R}}_{\mathbf{xx}}$  can be then obtained as:

$$\hat{\mathbf{R}}_{\mathbf{xx}} = \frac{1}{K} \sum_{k=1}^K x(t_k)x^H(t_k) = \frac{1}{K}\mathbf{X}\mathbf{X}^H \quad (2.4)$$

This matrix fundamentally encapsulates spatial information regarding the directions of incoming signals and serves as the cornerstone for all Direction of Arrival (DoA) algorithms, which are designed to extract this information.

## 2.2 Beamforming techniques

Given the knowledge of an array steering vector, the antenna array can be steered into a desired direction without the need of any mechanical components. Every time the array changes orientation, an average power at the array's output is measured. If the direction happens to coincide with the direction of the incoming signal, the average output power shall be at its maximum. The array pattern can be modified to further increase the precision of the estimations. This is achieved by designing a so-called weight vector  $\mathbf{w}$ , which represents a vector of complex numbers defining the amplitude and phase shifts at each element of the array, essentially shaping the radiation pattern. The weight vector is then linearly combined with the signal received by the array elements, forming an output signal  $y(t)$ ,

$$y(t) = \mathbf{w}^H\mathbf{x}(t) \quad (2.5)$$

The total averaged output power over  $N$  snapshots is given by:

$$P(\mathbf{w}) = \frac{1}{N} \sum_{n=1}^N |y(t_n)|^2 = \mathbf{w}^H \mathbf{x}(t_n) \mathbf{x}^H(t_n) \mathbf{w} = \mathbf{w}^H \hat{\mathbf{R}}_{xx} \mathbf{w} \quad (2.6)$$

Each estimation technique discussed in this chapter employs a distinct weight vector  $\mathbf{w}$ , tailored to achieve optimal DoA resolution for a required use case.

## 2.2.1 Bartlett's beamformer

In the Bartlett's beamforming approach, also known as delay-and-sum approach [1] or conventional beamforming approach [5][6], an array scan is conducted over a specified angular region of interest. The weighing vector  $\mathbf{w}$  corresponds to an array steering vector  $\mathbf{a}(\theta)$ , which is analogous to the array steering vector in 1.1. Here, angle  $\theta$  represents an arbitrary angle within the investigated angular region. Hence, the applied weighing vector shall be denoted as:

$$\mathbf{w} = \mathbf{a}(\theta) = [1 \quad e^{j\mu} \quad \dots \quad e^{j(M-1)\mu}]^T \quad (2.7)$$

with the spatial frequency  $\mu = -\frac{2\pi}{\lambda} \Delta \sin \theta$ .

The resulting power at the array's output can be computed following the equation 2.6. Let the signal generated by the  $i$ -th source impinge the array under an angle  $\theta_i$ . When  $\theta = \theta_i$ , phases of signal components on the array's elements align, which leads to the constructive combination of signals. Consequently, the output power reaches its maximum. The weight vector's magnitude may vary in respect to the angle  $\theta$ , affecting the total output power. To address this, normalisation is employed as follows:

$$\mathbf{w}_{\text{CON}} = \frac{\mathbf{a}(\theta)}{\sqrt{\mathbf{a}^H(\theta) \mathbf{a}(\theta)}} \quad (2.8)$$

This adjustment allows the variation in the output power to reflect the spatial alignment more accurately between the array and the incoming signal. The resulting output power is given by:

$$P_{\text{CON}}(\theta) = \frac{\mathbf{a}^H(\theta) \hat{\mathbf{R}}_{xx} \mathbf{a}(\theta)}{\mathbf{a}^H(\theta) \mathbf{a}(\theta)} \quad (2.9)$$

The metric  $P(\theta)$  is commonly referred to as the spatial spectrum. In case of ULA with isotropic elements, the magnitude of any element is inherently unity for any  $\theta$ , rendering the effects of varying magnitude irrelevant. Nevertheless, normalisation becomes crucial in practical implementations, where real arrays might exhibit varying gain across the scanned region due to their non-uniform radiation patterns.

This technique uses all available degrees of freedom to form a beam in a particular scan direction, which imposes constraints on resolution. This shortcoming

becomes particularly notable in the presence of multiple signals arriving from different directions. The spatial spectrum gets considerably distorted, given that both the beamwidth and side-lobes contribute to the measured output power for each scan direction. The resolution can be increased through the integration of additional array elements. Nonetheless, this approach comes with increased costs and puts higher demands on computational power.

## 2.2.2 MVDR

The Capon's beamformer [6][9], also known as the Minimum Variance Distortionless Response (MVDR) beamformer [5], employs the array's degrees of freedom not only to form the beam in the scan direction but also to nullify interference from undesired directions. The signal in the scan direction is passed with a constant gain, which is typically set to unity. The overall contribution of interfering signals to the total averaged output power is minimised. Such operational premise establishes a constrained optimisation problem, which can be solved using the method of Lagrange multipliers [10]. The weight vector is determined as follows:

$$\mathbf{w}_{\text{CAP}} = \frac{\hat{\mathbf{R}}_{xx}^{-1} \mathbf{a}(\theta)}{\mathbf{a}^H(\theta) \hat{\mathbf{R}}_{xx}^{-1} \mathbf{a}(\theta)} \quad (2.10)$$

Upon substituting into equation 2.6, the spatial spectrum is given by:

$$P_{\text{CAP}}(\theta) = \frac{1}{\mathbf{a}^H(\theta) \hat{\mathbf{R}}_{xx}^{-1} \mathbf{a}(\theta)} \quad (2.11)$$

The beam formed in the scan direction becomes much narrower, substantially reducing the contribution of side-lobes to  $P_{\text{CAP}}(\theta)$ . The primary limitation of this method is directly linked to its main advantage. The method relies on exploiting the correlation between interfering signals to reduce the total output power without the employment of spatial nulling. In the presence of two or more correlated signals of interest, these signals are combined destructively, rendering them undetectable. It can be shown, that  $\hat{\mathbf{R}}_{xx}$  becomes singular for correlated signals. Furthermore, the computational effort required to compute the inverse matrix increases with the array's scale, which can get expensive.

## 2.2.3 Linear prediction

In the Linear Prediction (LP) method [6][11], the objective is to minimise the total averaged output power by designing a weight vector such that the gain is unity for a specifically chosen element. The selection of this element is crucial as it significantly influences the overall resolution capability of the estimation. Unfortunately,

there are no definitive criteria for making this selection. The resolution is primarily affected by the SNR and the spatial distribution of the sources of the signals of interest. The weight vector is defined as:

$$\mathbf{w}_{\text{LP}} = \frac{\hat{\mathbf{R}}_{xx}^{-1} \mathbf{u}}{\mathbf{u}^H \hat{\mathbf{R}}_{xx}^{-1} \mathbf{u}} \quad (2.12)$$

where  $\mathbf{u}$  is a column vector representing the positions of elements within the array. This vector contains zeros at all positions except for the one corresponding to the selected element, which is marked by a value of 1. The spatial spectrum is calculated as:

$$P_{\text{LP}}(\theta) = \frac{\mathbf{u}^H \hat{\mathbf{R}}_{xx}^{-1} \mathbf{u}}{|\mathbf{u}^H \hat{\mathbf{R}}_{xx}^{-1} \mathbf{a}(\theta)|^2} \quad (2.13)$$

This method is particularly effective in scenarios where signals of interest arrive at the array with roughly equal strength and are nearly coherent. Under these conditions, it performs well even in environments with moderately low SNR.

## 2.3 Subspace-based techniques

Subspace-based techniques exploit the intrinsic properties of the matrix space defined by the  $M \times N$  covariance matrix  $\mathbf{R}_{\mathbf{xx}}$ , originating from the input data model (see equation 1.10). As outlined in [6], a unitary matrix  $\mathbf{U}$  can be chosen such that the  $d$  dimensional column space of  $\mathbf{R}_{\mathbf{xx}}$  is spanned by a subset of  $d$  columns of  $\mathbf{U}$ . Columns of  $\mathbf{U}$ , are thus linearly independent. Accordingly,  $d$  columns thus form the matrix  $\mathbf{U}_{\mathbf{s}}$ , the columns of which span the nonparallel (signal) subspace of  $\mathbf{R}_{\mathbf{xx}}$ . The remaining  $M - d$  columns form matrix  $\mathbf{U}_{\mathbf{o}}$ , the columns of which span the parallel (noise) subspace.

The ability to estimate the DoA relies on the following essential properties of  $\mathbf{R}_{\mathbf{xx}}$ :

1. The space spanned by eigenvectors of  $\mathbf{R}_{\mathbf{xx}}$  can be partitioned into two orthogonal subspaces: the signal subspace and the noise subspace.
2. Eigenvectors associated with larger eigenvalues of  $\mathbf{R}_{\mathbf{xx}}$  span the signal subspace, and directly relate to directions of impinging signals.
3. The steering vectors are contained within the signal subspace.
4. Eigenvectors associated with smaller eigenvalues of  $\mathbf{R}_{\mathbf{xx}}$  span the noise subspace.

Decomposing  $\mathbf{R}_{\mathbf{xx}}$  into two complementary subspaces is achieved through either Singular Value Decomposition (SVD) or Eigenvalue Decomposition (EVD). While SVD is more mathematically robust and offers high-resolution differentiation from the noise space, it is more computationally demanding than EVD. Additionally,

SVD yields more information than necessary for algorithms working solely with the eigenstructure of the covariance matrix, bypassing the need for left and right singular vector decomposition.

### 2.3.1 MUSIC

The MUSIC algorithm is a high-resolution multiple signal classification technique. It leverages the eigenstructure of the input covariance matrix for estimation of signal parameters, which provide information about the number of impinging signals, their cross-correlation, DoA, signal strengths, noise power, and more. Despite its high resolution, the algorithm necessitates precise array calibration. Any discrepancies result in a distortion of the spatial spectrum, due to a larger mismatch between steering vectors.

As outlined in [6], when  $D$  signals impinge on an  $M$ -element array, the data column vector can be expressed as:

$$\mathbf{x}(t) = \mathbf{A}\mathbf{s}(t) + \mathbf{n}(t) \quad (2.14)$$

$\mathbf{A}$  is the array steering matrix composed of the steering vectors  $a(\theta_j)$ , each corresponding to the DoA of the  $j$ -th signal,  $\mathbf{s}(t)$  is the vector of impinging signals and  $\mathbf{n}(t)$  is the noise vector. Going forward, the argument of vectors  $\mathbf{x}$ ,  $\mathbf{s}$  and  $\mathbf{n}$  will be omitted.

In geometric terms, vectors  $\mathbf{x}$  and  $a(\theta_j)$  reside within the  $M$ -dimensional space.  $\mathbf{A}$  has a full column rank, indicating that all steering vectors are linearly independent. The correlation matrix  $\mathbf{R}_{\mathbf{xx}}$  is formulated as:

$$\mathbf{R}_{\mathbf{xx}} = E\{\mathbf{xx}^H\} = AE\{\mathbf{ss}^H\}\mathbf{A}^H + E\{\mathbf{nn}^H\} = \mathbf{A}\mathbf{R}_{\mathbf{ss}}\mathbf{A}^H + \sigma_N^2\mathbf{I} \quad (2.15)$$

where  $\mathbf{R}_{\mathbf{ss}}$  is the signal covariance matrix, which is non-singular when impinging signals are not highly correlated. The eigenvalues  $\{\lambda_1, \dots, \lambda_M\}$  of  $\mathbf{R}_{\mathbf{xx}}$  can be obtained from:

$$|\mathbf{R}_{\mathbf{xx}} - \lambda_i\mathbf{I}| = 0 \quad (2.16)$$

An arbitrary eigenvector  $q_i$ , associated with eigenvalue  $\lambda_i$ , is derived from the equation:

$$(\mathbf{R}_{\mathbf{xx}} - \lambda_i\mathbf{I})q_i = 0 \quad (2.17)$$

The substitution of 2.6 into 2.16 yields:

$$|\mathbf{A}\mathbf{R}_{\mathbf{ss}}\mathbf{A}^H + \sigma_N^2\mathbf{I} - \lambda_i\mathbf{I}| = |\mathbf{A}\mathbf{R}_{\mathbf{ss}}\mathbf{A}^H - (\lambda_i - \sigma_N^2)\mathbf{I}| = 0 \quad (2.18)$$

Thus, the eigenvalues can be substituted for  $\nu_i$ , such that:

$$\nu_i = \lambda_i - \sigma_N^2 \quad (2.19)$$

From linear algebra, it is established that a matrix  $\mathbf{A}$  with a full column rank, combined with non-singular  $\mathbf{R}_{\text{ss}}$ , ensures that the  $M \times M$  matrix  $\mathbf{A}\mathbf{R}_{\text{ss}}\mathbf{A}^H$  is a positive semi-definite of rank  $D$ , provided that the number of impinging signals  $D$  is less than the number of array elements  $M$ . Consequently,  $M - D$  eigenvalues  $\nu_i$  of  $\mathbf{A}\mathbf{R}_{\text{ss}}\mathbf{A}^H$  must be zero. This condition implies that the eigenvalues  $\lambda_{D+1}, \dots, \lambda_M$  of  $\mathbf{R}_{\text{xx}}$  must equal  $\sigma_N^2$ . However, given that  $\mathbf{R}_{\text{xx}}$  is estimated from a finite data sample, these eigenvalues will not be precisely identical but will form a closely spaced cluster, with the mean value approaching  $\sigma_N^2$ . An increase in the number of data samples results in a decrease in the variance of these eigenvalues. The smallest eigenvalue is employed as reference. The reference eigenvalue is then used to determine multiplicity  $K$  of eigenvalues spanning the noise subspace. The number of estimated signals can be then obtained as:

$$\hat{D} = M - K \quad (2.20)$$

In practice, determining the multiplicity of  $K$  presents a challenge, prompting the development of various methods for estimating the number of signals (see 2.6). Substituting 2.6 into 2.17, eigenvectors associated with the noise subspace are identified as:

$$(\mathbf{A}\mathbf{R}_{\text{ss}}\mathbf{A}^H + \sigma_N^2\mathbf{I} - \lambda_i\mathbf{I})q_i = (\mathbf{A}\mathbf{R}_{\text{ss}}\mathbf{A}^H + \sigma_N^2\mathbf{I} - \sigma_N^2\mathbf{I})q_i = 0 \quad (2.21)$$

$$\mathbf{A}\mathbf{R}_{\text{ss}}\mathbf{A}^H q_i = 0 \quad (2.22)$$

The full rank  $\mathbf{A}$  and the non-singular  $\mathbf{R}_{\text{ss}}$  imply that:

$$\mathbf{A}^H q_i = \begin{bmatrix} a(\mu_1)q_i \\ \vdots \\ a(\mu_D)q_i \end{bmatrix} = \begin{bmatrix} 0 \\ \vdots \\ 0 \end{bmatrix} \quad (2.23)$$

From 2.23 it is evident, that eigenvectors associated with the smallest eigenvalues must be orthogonal to the steering vectors of  $\mathbf{A}$ .

$$\{a(\mu_1), \dots, a(\mu_D)\} \perp \{q_{D+1}, \dots, q_M\}$$

This condition allows for an estimation of  $\mathbf{A}$  just by identifying steering vectors that are orthogonal to eigenvectors spanning the noise subspace. The estimated steering matrix  $\hat{\mathbf{A}}$  directly corresponds to the DoA of impinging signals. To find the steering vectors, a matrix  $\mathbf{V}_{\mathbf{n}}$  is formed by eigenvectors spanning the noise subspace:

$$\mathbf{V}_{\mathbf{n}} = [q_{D+1} \quad \dots \quad q_M] \quad (2.24)$$

It can be shown that for any scanning angle  $\theta$  from a set of angles  $\{\theta_1, \dots, \theta_D\}$  corresponding DoA of impinging signals:

$$a(\theta)^H \mathbf{V}_{\mathbf{n}} \mathbf{V}_{\mathbf{n}}^H a(\theta) = 0 \quad (2.25)$$



The DoA is estimated by scanning across the area of interest and calculating the spatial spectrum given by:

$$P_{\text{MUSIC}}(\theta) = \frac{1}{a(\theta)^H \mathbf{V}_n \mathbf{V}_n^H a(\theta)} \quad (2.26)$$

Or, alternatively,

$$P_{\text{MUSIC}}(\theta) = \frac{a(\theta)^H a(\theta)}{a(\theta)^H \mathbf{V}_n \mathbf{V}_n^H a(\theta)} \quad (2.27)$$

The orthogonality between  $a(\theta)$  and  $\mathbf{V}_n$  will minimise the denominator in the equation, resulting in  $\hat{D}$  largest peaks in the spectrum corresponding to DoA of impinging signals. However, in the presence of highly correlated signals the algorithm fails. The correlation leads to a singular  $\mathbf{R}_{ss}$ , undermining the foundational orthogonality between the signal and noise subspaces.

Furthermore, improper calibration of the array complicates the estimation of steering vectors, causing a discrepancy between the estimated steering vectors and the actual steering vectors contained in  $\mathbf{A}$ . This misalignment results in a reduction of peaks in the spatial spectrum, as  $a(\theta)^H \mathbf{V}_n \mathbf{V}_n^H a(\theta)$  generates higher values, indicating a weakened ability to distinctly identify signal directions.

### 2.3.2 Root-MUSIC

The Root-MUSIC algorithm has been proposed in [12][1] as an improvement to the original MUSIC algorithm. Unlike MUSIC, which involves generating array steering vectors across a spectrum of angles to calculate the spatial spectrum and identify peaks for determining the DoA, Root-MUSIC simplifies the process by directly computing the angles. The MUSIC spatial spectrum, given by equation 2.26, is an all-pole function. By solving for the poles, angles corresponding to DoA are obtained. The algorithm is particularly effective with ULAs due to their straightforward steering vector configurations.

A polynomial is derived as follows:

$$\mathbf{J}(z) = a(z)^H \mathbf{V}_n \mathbf{V}_n^H a(z) \quad (2.28)$$

Here, evaluating the MUSIC spectrum  $P_{\text{MUSIC}}(\theta)$  then becomes equivalent to evaluating the polynomial  $J(z)$  on the unit circle. The array steering vector for ULA is expressed as:

$$a(z) = \left[ 1 \quad z^{-1} \quad \dots \quad z^{-(M-1)} \right]^T \quad (2.29)$$

where  $z = e^{-j \frac{2\pi\Delta}{\lambda} \sin \theta}$  (see chapter 1.1). The polynomial's roots encapsulate information about the DoA of the impinging signals. In an ideal, noise-free environment, the roots would lie directly on the unit circle. Following assumptions made in [reference

number of estimated signal in the MUSIC algorithm], in practice, it is assumed that  $\hat{D}$  number of roots,  $z_k$ , closest to the unit circle correspond to impinging signals. The incident angles of individual signals are obtained from equation:

$$\theta_k = \arcsin \left[ \frac{\lambda}{2\pi d} \arg(z_k) \right] \quad (2.30)$$

The algorithm has demonstrated superior resolution compared to the traditional MUSIC algorithm, making it especially useful in low SNR environments. Furthermore, it offers reduced computational complexity, particularly when employed with simple array configurations.

### 2.3.3 Min-norm MUSIC

The minimum norm algorithm [6][13] is categorised within the weighted MUSIC algorithms, aimed at enhancing resolution in environments characterised by low SNR and scenarios of limited availability of data samples. The calculation of the spatial spectrum incorporates a weighing matrix  $\mathbf{W}$ , introduced to adjust the contribution of each eigenvector spanning the noise subspace, allowing for preferential amplification of certain spatial directions, potentially improving resolution. The spatial spectrum is obtained as:

$$P_{\text{WMUSIC}}(\theta) = \frac{1}{a(\theta)^H \mathbf{V}_n \mathbf{V}_n^H \mathbf{W} \mathbf{V}_n \mathbf{V}_n^H a(\theta)} \quad (2.31)$$

It is evident that setting  $\mathbf{W} = \mathbf{I}$  transforms the spectral estimation back into the original MUSIC algorithm, with the exception that the denominator is squared, resulting in an overall increase in output power levels.

The minimum norm algorithm specifically configures the first element of  $W$  to unity by defining:

$$\mathbf{W} = e_1 e_1^T \quad (2.32)$$

Here,  $e_1$  is the first column of an  $M \times M$  identity matrix, applicable to an  $M$ -element ULA. Such a selection of  $W$  leads to an increase in asymptotic variance, resulting in broader peaks. Nonetheless, as proven in [14], the algorithm exhibits low bias, thereby achieves higher precision in DoA estimation for ULAs.

## 2.4 Maximum likelihood techniques

Maximum Likelihood (ML) techniques [6][1][8] are characterised by their superior performance, especially in low SNR environments and with small data sample sizes. They outperform all subspace-based algorithms in effectiveness, maintaining their

reliability even in the presence of correlated signals. However, their substantial computational demands often make more efficient techniques favourable, despite being less robust.

The aim of these techniques is to reconstruct the output data vector  $x(t_n)$  in such way, that allows for identification of the steering matrix  $\mathbf{A}(\hat{\theta})$  and the signal vector  $s(t_n)$ . Parameters  $\hat{\theta}$  and  $\hat{s}(t_n)$  are estimated through an iterative process. The product  $\mathbf{A}(\hat{\theta})\hat{s}(t_n)$  is then subtracted from data  $x(t_n)$  and the residual evaluated. If the estimate is sufficiently accurate, the residual will predominantly consist of noise and interference. Consequently, by minimising the energy of the residual  $x(t_n) - \mathbf{A}(\hat{\theta})\hat{s}(t_n)$  through the appropriate selection of  $\hat{\theta}$  and  $\hat{s}(t_n)$ , it can be assumed that  $\hat{\theta} \approx \theta$  and  $\hat{s}(t_n) \approx s(t_n)$ . This leads to the formulation of a minimisation problem:

$$\min_{\hat{\theta}, \hat{s}(t_n)} \left\{ \sum_{n=0}^{N-1} |x(t_n) - \mathbf{A}(\hat{\theta})\hat{s}(t_n)|^2 \right\} \quad (2.33)$$

Fixing  $\hat{\theta}$  and minimising with respect to  $\hat{s}(t_n)$ , the least squares solution is derived as:

$$\hat{s}(t_n) = [\mathbf{A}^H(\hat{\theta})\mathbf{A}(\hat{\theta})]^{-1} \mathbf{A}^H(\hat{\theta})x(t_n) \quad (2.34)$$

Substituting the equation above back into the minimisation problem allows  $\hat{\theta}$  to be characterised as maximising a matrix trace:

$$\max_{\hat{\theta}} \text{trace} \left\{ P_{\mathbf{A}(\hat{\theta})} \mathbf{R}_{\mathbf{xx}} \right\} \quad (2.35)$$

Here,  $P_{\mathbf{A}(\hat{\theta})}$  is the projection matrix, which projects vectors onto the space spanned by columns of  $\mathbf{A}(\hat{\theta})$  and is defined as:

$$P_{\mathbf{A}(\hat{\theta})} = \mathbf{A}(\hat{\theta}) [\mathbf{A}^H(\hat{\theta})\mathbf{A}(\hat{\theta})]^{-1} \mathbf{A}^H(\hat{\theta}) \quad (2.36)$$

Maximising the trace of the matrix  $P_{\mathbf{A}(\hat{\theta})} \mathbf{R}_{\mathbf{xx}}$  leads to the assumption that  $\hat{\theta}$  asymptotically approaches the real angle  $\theta$ .

## 2.5 Signal preprocessing techniques

When estimating DoA in real-world environments, signals often experience multipathing, where they reflect off obstacles and impinge the array from various angles. In such cases, impinging signals exhibit some form of coherence or covariance. Subspace-based algorithms rely heavily on the covariance matrix  $\mathbf{R}_{\mathbf{xx}}$  having rank equal to the number of impinging signals. In the presence of coherent or covariant signals, these algorithms fail to properly partition eigenvectors into noise and signal subspaces, rendering estimations inaccurate. Preprocessing schemes have been developed to reduce or eliminate the impact of correlated and coherent signals on the rank of  $\mathbf{R}_{\mathbf{xx}}$  by essentially decorrelating the signals before further processing.

## 2.5.1 Forward-backward averaging (FBA)

This technique is applicable to centro-symmetric arrays, which can be flipped around its origin without affecting the radiation pattern. In such arrays, steering vectors remain unchanged when the positions of elements are flipped, and signals received on these elements are conjugated. This property can be exploited to artificially increase the rank of the signal covariance matrix  $\mathbf{R}_{\text{ss}}$  (see 2.2) by one without affecting the phase relations connected to steering vectors. The flipped conjugated copy of the original data simulates a reception of time-inverted replica of the original data, effectively reversing the phase in the complex plane, which disrupts the correlation between phases of impinging signals. Let  $\mathbf{X}$  be the data matrix of size  $M \times N$ . The extended data matrix  $\mathbf{Z}$  can then be obtained as:

$$\mathbf{Z} = \begin{bmatrix} \mathbf{X} & \mathbf{\Pi}_M \bar{\mathbf{X}} \mathbf{\Pi}_N \end{bmatrix} \quad (2.37)$$

Where  $\mathbf{\Pi}_M$  and  $\mathbf{\Pi}_N$  are square exchange matrices used to flip the order of data samples. An exchange matrix  $\mathbf{\Pi}_M$  is of size  $M \times M$  and takes the following form:

$$\mathbf{\Pi}_M = \begin{bmatrix} 0 & 0 & \cdots & 0 & 1 \\ 0 & 0 & \cdots & 1 & 0 \\ \vdots & \vdots & \ddots & \vdots & \vdots \\ 0 & 1 & \cdots & 0 & 0 \\ 1 & 0 & \cdots & 0 & 0 \end{bmatrix} \quad (2.38)$$

The extended covariance matrix (see 2.4) is calculated as follows:

$$\mathbf{R}_{\text{xx}}^{\text{FBA}} = \frac{1}{2N} \mathbf{Z} \mathbf{Z}^H = \frac{1}{2N} (\mathbf{X} \mathbf{X}^H + \mathbf{\Pi}_M (\mathbf{X} \mathbf{X}^H)^* \mathbf{\Pi}_M) \quad (2.39)$$

The resulting matrix  $\mathbf{R}_{\text{xx}}^{\text{FBA}}$  is mirrored around its inverse diagonal. In case of centro-symmetric arrays, the covariance matrix still retains all the information about phase relations between signals received by individual elements. However, its structure is altered, so when two correlated or coherent signals impinge the array from two distinct directions, the covariance of the original data does not perfectly align with the covariance of its flipped time-reversed version. Effects of the coherence (or correlation) are spread more evenly across the whole correlation matrix  $\mathbf{R}_{\text{xx}}^{\text{FBA}}$ .

As mentioned earlier, this method can increase the rank of  $\mathbf{R}_{\text{ss}}$  by one, thus works well in the presence of two coherent or correlated signals. In scenarios with more signals, the FBA is unable to introduce enough phase component diversity to effectively decorrelate these signals.

## 2.5.2 Spatial smoothing

In spatial smoothing [6] the array is divided into multiple sub-arrays that process incoming signals independently. These sub-arrays may even overlap. The covariance

matrix for each sub-array is calculated, and in the end, these matrices are summed and averaged. This method enables signals to be analysed from slightly different perspectives.

A practical example of spatial smoothing can be demonstrated with a  $M$ -element ULA, impinged by  $d$  signals each coming from a different direction, among which  $k$  signals are covariant. The signal covariance matrix  $\mathbf{R}_{\mathbf{ss}}$  will have a rank of  $d - k$ . Consequently,  $\mathbf{R}_{\mathbf{xx}}$  will also have a rank of  $d - k$ , causing subspace-based methods to fail in accurately identifying directions of these coherent signals. The ULA can be divided into  $L$  sub-arrays, each with  $M_{\text{sub}} = M - L + 1$  elements as shown on Figure 2.1. The array division can be done in both directions.

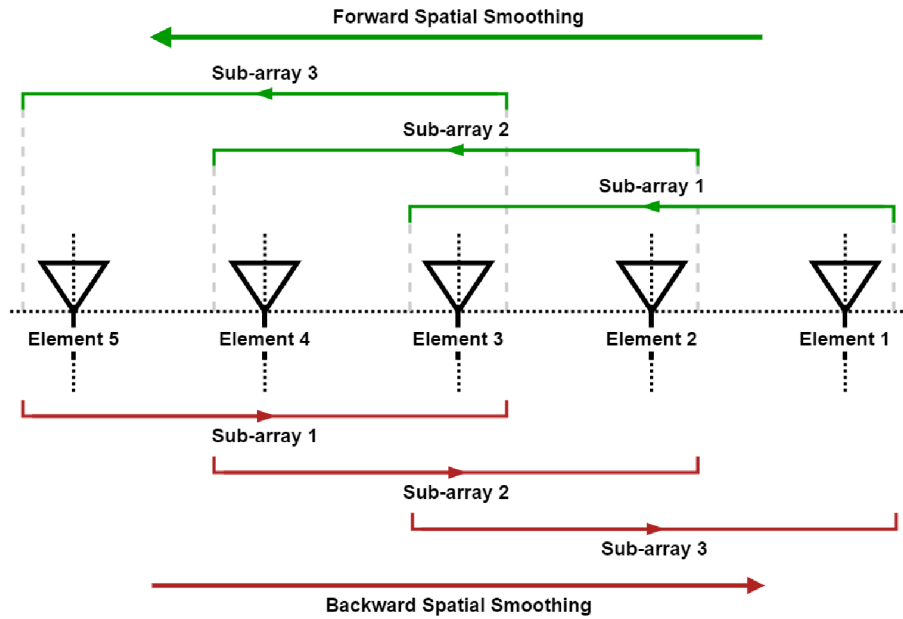


Fig. 2.1: Sub-array division of ULA for forward and backward spatial smoothing.

The data matrix for each  $l$ -th sub-array is obtained as:

$$\mathbf{X}_l = \mathbf{J}_l \mathbf{X} \quad (2.40)$$

Where the selection matrix  $\mathbf{J}_l = [0 \quad \mathbf{I}_{M_{\text{sub}}} \quad 0]$  of size  $M_{\text{sub}} \times M$  is used to select rows of samples relevant to the  $l$ -th subarray. The spatially smoothed data matrix  $\mathbf{Z}$  then composed as:

$$\mathbf{Z} = [\mathbf{J}_1 \mathbf{X} \quad \mathbf{J}_2 \mathbf{X} \quad \cdots \quad \mathbf{J}_L \mathbf{X}] \quad (2.41)$$

The spatially smoothed covariance matrix of size  $M_{\text{sub}} \times M_{\text{sub}}$  is obtained as:

$$\mathbf{R}_{\mathbf{xx}}^{\text{ss}} = \frac{1}{NL} \mathbf{Z} \mathbf{Z}^H = \frac{1}{NL} \sum_{l=1}^L \mathbf{J}_l^T (\mathbf{X} \mathbf{X}^H) \mathbf{J}_l \quad (2.42)$$

The number of samples increases from  $N$  to  $N \times L$ , which helps to further smooth out the covariance matrix. Although the covariance matrix  $\mathbf{R}_{\mathbf{xx}}^{\text{ss}}$  attains the required

rank  $d$ , the effective array size is reduced from  $M$  to  $M_{\text{sub}}$  elements. Therefore, to detect  $d$  number of signals, each sub-array must have at least  $M_{\text{sub}} = d + 1$  elements. Moreover, if  $k$  signals are coherent, each sub-array should contain at least  $2k$  elements to correctly resolve inter-signal correlations.

Unlike FBA, this method is not restricted to centro-symmetric arrays and is applicable to any array configuration. When the sub-array division starts from the rightmost element, the method is termed “forward spatial smoothing”. Conversely, when starting from the leftmost element, it is referred to as “backward spatial smoothing”. The choice of which method to use for better performance solely depends on the specific array configuration. Nonetheless, optimal results are typically achieved by averaging both forward and backward directions, a method known as “forward-backward spatial smoothing” (FB-SS). This method has also been shown to reduce the number of elements required to estimate  $k$  coherent signals from the originally needed  $2k$  to  $1.5k$ . However, these advantages come with the cost of increased overall computational complexity of the preprocessing method.

## 2.6 Model order estimation

Up until now, it was assumed that the number of signals present in the data sample is known. However, in practice, the number of impinging signals is generally unknown. Since the accurate identification of the number of signals is critical for operation of all subspace-based and maximum likelihood methods, these estimations must be conducted prior to the implementation of DoA estimation algorithms. These techniques are commonly referred to as model order estimations.

The simplest approach to estimating the number of signals involves analysing the eigenspace of the data covariance matrix (as in 2.4), where the eigenvalues belonging to the signal subspace are considerably larger than those belonging to the noise subspace. The model order estimate can then be obtained by estimating the multiplicity  $k$  of eigenvalues spanning the noise subspace. In theory, these small eigenvalues should all be equal to the noise variance  $\sigma_N^2$ . By setting a threshold to determine these values, the model order estimate  $\hat{D}$  can be obtained as in 2.20:

$$\hat{D} = M - k \quad (2.43)$$

In reality, the presence of non-uniform, time-variant noise and broadband interferences results in considerable variation in the smaller eigenvalues, which then form a closely spaced cluster around the hypothetical  $\sigma_N^2$ . Although increasing the data sample size can potentially reduce this variance, estimation based on a fixed threshold is not often effective. Consequently, various statistical tests have been developed that have proven to yield more accurate results.

## 2.6.1 Minimum descriptive length criterion

The Minimum Descriptive Length (MDL) criterion [8], widely used in array signal processing, presents a minimisation problem, designed to determine the most statistically probable model order such as [cite intro to DoA][cite Optimum Array Processing]. The minimisation formula can be written as:

$$\min_d \left\{ -\log \left( \frac{\prod_{i=d+1}^M \lambda_i^{\frac{1}{M-d}}}{\frac{1}{M-d} \sum_{i=d+1}^M \lambda_i} \right) + \frac{1}{2} \hat{p}(k) \log N \right\} \quad (2.44)$$

Where  $M$  is the number of elements in the array,  $d \in \{0, 1, \dots, M-1\}$  represents the number of estimated signals,  $N$  is the number of samples,  $\lambda_i$  are the eigenvalues of the covariance matrix and  $\hat{p}(k)$  denotes the penalty function.

The model order is determined by calculating the MDL for all potential values of  $d$  and identifying the value that yields the smallest MDL. The calculation involves two components: the log-likelihood function and the penalty function. As  $d$  increases, one additional eigenvalue is excluded from the evaluation, and the value of the log-likelihood function decreases. The penalty function imposes a statistical weight on the criterion, influenced by the properties of the covariance matrix and the preprocessing methods applied. Its value increases with  $d$ .

$$\hat{p}(k) = \begin{cases} d(2M - d + 1) & \text{for real matrices} \\ d(M + d + 1) & \text{for real matrices with preprocessing} \\ 0.5d(2M - d) & \text{for complex matrices} \\ 0.5d(2M - d + 1) & \text{for complex matrices with preprocessing} \end{cases} \quad (2.45)$$

When  $d$  is equal to the number of large eigenvalues, meaning all large eigenvalues are dropped from the ensemble, the criterion shall yield minimum. This obviously depends on the power of the impinging signals. As signal power decreases to and below noise levels the method becomes more and more unreliable as the noise and signal subspaces become less distinct. In case of coherent signals, preprocessing methods must be used exactly for the same reason.

### 3 Software-defined radio

The primary objective of a communication system is to transfer information (text, voice, video, or data) from the sender to the recipient across a distance both effectively and efficiently. Effectiveness in this context refers to the system's capacity to transfer information quickly and with high accuracy. Efficiency, on the other hand, denotes the system's ability to utilise available resources such as bandwidth and power. The underlying technology enabling this transfer is broadly classified under the category of radio systems. These systems form an information processing chain that incorporates both digital and analog methods. A block diagram of a general communication system is shown in Figure 3.1.

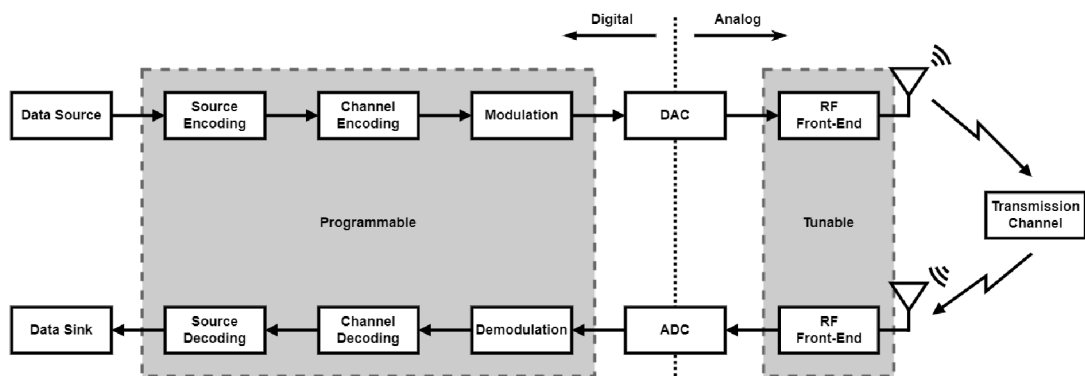


Fig. 3.1: Block diagram of a general communication system.

At the transmitter, the binary data is processed by removing redundancy and incorporating error protection, subsequently converting the binary sequence into an electromagnetic sinusoidal waveform uniquely defined by distinct physical characteristics such as carrier frequency, signal amplitude, and phase. This transformation involves digital processing at the baseband level and analog processing at the RF Front-End (RFFE), where signals are up-converted from baseband to passband. These signals travel through a transmission channel that introduces noise and signal distortion. Upon reception at the receiver, the physical characteristics of the distorted waveform are identified. The received signal undergoes down-conversion to the baseband, followed by the extraction of the binary sequence and error correction. A more detailed explanation of a general communication system processing chain is provided in [15].

Over the past several decades, advancements in hardware and DSP have enabled radios to implement most, if not all, baseband operating functions through software. Furthermore, the modern hardware allows for much more flexible RFFE. Individual components are repurposed and reconfigured supporting a wide range of applications



and enabling adjustments to changes in the transmission channel. These technological advancements have collectively led to the development of the Software Defined Radio (SDR) platform.

An SDR is a complex system performing multiple complicated tasks concurrently, ensuring seamless data transmission and reception while allowing software-based adjustments to meet application-specific requirements. The term “software defined” refers to the use of software to implement operating functions. The objective of an SDR is to establish a versatile platform by incorporating as much software control into the RFFE architecture as feasible. This involves replacing static components with tunable alternatives, resulting in a system with high frequency and bandwidth flexibility. Such versatility allows for high performance across various applications that would traditionally require separate RF solutions. However, the versatility of an SDR remains bound by factors such as size, cost, power consumption, etc. Consequently, it is crucial to understand the limitations of specific SDR platforms and the effect of design parameters on the overall performance necessary for the intended application.

### **3.1 RF architectures**

SDR systems usually implement transceiver architectures. However, certain DSP applications may only require the receiving chain when no transmission of information is required. This is also true for the isolated case of Direction of Arrival (DoA) estimation, where no subsequent transmission of data is needed. Henceforth, more detailed attention is given to the description of the receiver. An effective receiver must process the in-band information while rejecting any out-of-band interference. The signals are down-converted to the baseband, lowering the sampling frequency requirements for digital processing. This can be accomplished via various RF architectures. The common architectures, along with their limitations, are detailed in [4]. Additionally, [15] provides an overview of the most prominent types, specifically the superheterodyne and zero-IF architectures.

The superheterodyne architecture utilises single or dual intermediate frequency (IF) mixing stage for baseband down-conversion. Such configuration enables precise bandwidth and channel selectivity through a variable, multi-stage IF filter system. The distribution of gain across IF stages facilitates optimisation for either a low noise figure or improved system linearity. The multi-stage design also assists in suppressing the leakage of the local oscillator. Heterodyne architecture has been around since the 1900s and it has seen substantial improvements in performance. However, despite the general trend toward miniaturisation in RF components, the

high-performance IF filters used in these systems remain relatively large. Furthermore, careless design of the IF filters can result in the presence of images and mixing spurs in the baseband. Proper frequency planning is essential yet limits the system's versatility.

Over the last couple of decades, advancements in signal processing have allowed the zero-IF architecture to emerge as a superior alternative to the superheterodyne. Quadrature downconversion directly converts the signal to the baseband, essentially splitting it into its phase (I) and quadrature (Q) components. This method effectively eliminates effects of image frequencies and significantly reduces the influence of mixing spurs. Baseband filters are simpler, cheaper, and allow for a monolithic design. On the other hand, the architecture is susceptible to I/Q imbalance due to variations in manufacturing processes and temperature fluctuations in the signal processing chain, which complicate impedance matching. In addition, the imperfect isolation of the local oscillator leads to carrier leakage during the mixing stage. Nonetheless, the challenges associated with the zero-IF architecture are considerably more manageable compared to the filtering requirements of the superheterodyne, thereby rendering the zero-IF solution more feasible for next-generation systems.

## 3.2 Requirements for DoA estimation

DoA estimation represents a specialised application within DSP aimed at determining the direction from which a signal is received rather than extracting its binary information. This necessitates the utilisation of multi-channel systems, enabling the analysis of the received signals in the form of a data matrix, as demonstrated in 2.4. The versatile nature of the SDR platforms makes them particularly well-suited for such a purpose.

Multi-channel SDRs are equipped with multiple RFFEes for signal acquisition from separate elements of the antenna array. These acquired signals can then be processed in a shared digital processing chain. In some instances, SDRs may feature completely independent channels with separate RFFEes and digital processing chains. The requirement for multi-channel SDRs in DoA estimation arises from the underlying principle of estimation techniques, which strictly rely on the phase offsets introduced by the delay of the wavefront travelling between consecutive elements of the antenna array.

It is important to note that hardware components in the signal receiving chain introduce ambiguities to the received signals due to inherent variations. When RFFEes are not synchronised, frequency and timing offsets occur. Frequency offset originates from the separate frequency clocks of RFFEes responsible down-conversion, as they always suffer from some frequency instability. This may result in significant

frequency offsets between channels. The timing offset arises from the unsynchronised initiation of clock sources leading to inconsistent artificial timing delays between channels. To minimise the influence of these offsets on the DoA estimation accuracy, complete synchronisation must be ensured. Synchronisation can be achieved through the utilisation of common reference and clock signals or through in-software offset corrections. Under these circumstances the SDR can be considered channel coherent.

In addition to synchronisation, several other requirements must be met for effective DoA estimation. The system's time-variability must be minimised to ensure consistency across repeated experiments conducted in the same environment with identical operating parameters. The SDR must also allow for a fast reconfiguration through its software tools, facilitating easy prototyping and implementation of estimation algorithms. These estimations are usually performed in real time, requiring low latency and high computational throughput. The SDR's microprocessor must support these high computational demands; otherwise, the inadequate processing capabilities may result in spectral distortion or, in worst case, make the spatial spectrum calculation impossible.

The key parameters of the front-end to be considered when selecting an SDR for DoA estimation include:

- Frequency range: This range defines the operating frequency spectrum of an SDR.
- Bandwidth: It determines the width of the frequency band that can be processed concurrently. Wider bandwidths allow more detailed capture of signal characteristics, potentially improving the estimation accuracy.
- Analog-to-Digital Converter (ADC) resolution: The ADC converts the analog signal into the discrete-time domain necessary for DSP. The resolution determines how finely can the signal be quantized into its discrete-time digital representation. The resolution, defined in bits, affects how precisely the signal is quantized into its digital representation. The higher the resolution, the higher the ability to differentiate between weaker and stronger signals.
- Sample rate: Defines the frequency at which the ADC samples the analog signal, converting it into discrete-time domain.
- Number of channels: Increasing the number of channels enhances spatial spectrum resolution, yet it also increases demands on the digital processing chain and the required computational power.
- Noise figure: The figure characterises the amount of noise added by the SDR system to processed signals. A low noise figure is crucial for maintaining signal fidelity and sensitivity, especially in environments with high levels of interference.

## 4 Hardware & software setup

The successful implementation of the DoA estimation demonstrator relies on the selection of an SDR platform that balances performance, affordability, and practicality. A wide variety of professional multi-channel coherent SDRs available on the market are well-suited for such a task. The objective of this chapter is to first investigate the existing market offerings and then to identify a viable compromise that fulfils defined criteria while staying affordable due to constraints on available funding. Following criteria were defined for orientation when searching for a viable solution:

- **Cost:** The price of the hardware shall be kept at a minimum while enabling demonstration of the DoA estimation techniques.
- **Processing power:** The computational and processing capabilities of the chosen SDR platform are required to ensure sufficient precision and efficiency of the DoA estimation. It is expected that modern consumer-grade hardware can provide adequate processing power. The key parameters of the front-end identified in chapter 3.2 will guide the evaluation of these processing capabilities.
- **Availability:** The hardware shall be readily purchasable without unexpected delays and logistical hurdles. A widespread availability ensures ease of acquisition and fast scalability for future expansions.
- **Reliability:** The chosen SDR platform shall demonstrate acceptable reliability, particularly for long-term deployments and continuous operation, without significant performance degradation.
- **Form factor:** A compact design facilitates simpler integration into larger setups and allows for easy transportation.

### 4.1 Market research

#### USRP X300

The Ettus Research USRPs are widespread across many professional DSP research fields, recognised for their high performance and user-programmable FPGAs, which enable straightforward adaptation to specific application needs. They have been extensively utilised in numerous research papers focusing on DoA estimation, as evidenced by [16] [17]. However, it is important to note that these devices are often disregarded due to their high cost, and in this context, they are only referenced as an exemplary professional-grade platform for comparative purposes.

The USRP X300 serves as an entry point into the realm of scalable professional-grade SDR platforms commonly employed in research and development fields. Fea-

turing a 2-channel transceiver architecture with full-duplex capabilities, it covers a frequency range from DC to 6 GHz, with a baseband bandwidth up to 160 MHz. Equipped with a 14-bit resolution ADC, it offers sampling rates up to 200 MS/s. At the forefront of its signal processing capabilities is a programmable XC7K325T FPGA, supporting multiple high-speed interface options that enable transfer speeds up to 200 MS/s per RX channel.

While the X300 is initially limited to two RX channels, the number of channels can be increased by employing two USRP TwinRX daughter boards. With such configuration, four channels become available. However, this enhancement comes at the expense of halved sampling rate. An exemplary solution employing synchronisation methods for such a setup can be found in [18].

## **ADALM-PLUTO**

ADALM-PLUTO, also known as PlutoSDR, is a consumer-grade transceiver renowned for its practicality. Marketed as a prototyping/training platform for smaller developers, this SDR's architecture is based on the Analog Devices AD9363 chip and the Xilinx Zynq Z-7010 FPGA, which is commonly utilised in the professional field. This enables developers to streamline the conversion of the design to industrial or embedded format.

The PlutoSDR offers a frequency range spanning from 325 MHz to 3.8 GHz, with a maximum base-band bandwidth of 20 MHz. The ADC has 12-bit resolution, supporting sampling frequencies up to 65.1 kS/s. The SDR features only one RX channel.

Multiple SDRs can be synchronised to increase the number of available RX/TX channels. PlutoSDR rev.C supports synchronisation via shared external clock, allowing for implementation by daisy-chaining SDRs in series. Alternatively, synchronisation can be achieved using an off-the-shelf PCB. Additionally, Coherent Receiver provides a similar external synchronisation card tailored for the PlutoSDR, which is particularly advantageous for older revisions lacking support for external clock sources.

## **HackRF One**

HackRF is an open-source transceiver platform aimed at the development and testing of next-generation radio technologies. Launched via Kickstarter in 2014, it attracted not only radio amateurs, but also cybersecurity researchers, gradually establishing itself as a reliable platform for cybersecurity research. Its architecture relies on MAX2839 half-duplex transceiver, MAX5864 ADC/DAC from Analog Devices and NXP's LPC4320 ARM Cortex-M4 microcontroller.

HackRF One r9 features frequency range from 1 MHz to 6 GHz, maximum baseband bandwidth of 20 MHz and 8-bit ADC resolution and a sampling rate 20 MS/s. The SDR is equipped with a single RX and TX channel.

Similar to PlutoSDR, HackRF offers external clock support for time synchronisation. It enables distribution of the clock signal from the clock output port of one HackRF One to the clock input ports of other HackRFs. Additionally, synchronisation can be achieved by implementing additional clock signals from the on-board extension header, as proposed in [19]. The synchronisation pulse can be generated by one of the SDRs or by an external device such as a GNSS receiver, facilitating wireless synchronisation over a longer distance.

## **BladeRF**

BladeRF 2.0 micro stands as another open-source platform, sharing some of its functionalities with HackRF One. Its architecture is based on the AD9361 chip from Analog Devices and Intel's Cyclone V microcontroller. Available in two versions, namely the Ax4 and Ax9, the Ax9 variant offers enhanced computational throughput. The SDR's frequency range extends from 47 MHz to 6 GHz, with maximum baseband bandwidth of 56 MHz. It has a 12-bit ADC, supporting sampling rates up to 61.4 MS/s. It features two RX and TX channels. The BladeRF has the capability to provide its base clock to other devices, and it can also receive this clock signal from other external devices. However, the synchronisation of multiple BladeRF devices has not yet been thoroughly verified and would require further testing to ensure reliability and consistency.

## **RTL-SDR**

RTL-SDR stands out as the most widespread freely available amateur SDR on the market. Its architecture is built upon DVB-T USB receivers featuring the RTL2832U chip. In the course of 2012, a group of RF engineers discovered the chip's potential by exploiting its special mode of operation, thereby enabling its utilisation for broadband SDR applications. These receivers are now commonly priced around 25 dollars. With the help of custom software drivers, they can be easily converted into inexpensive SDR receivers, offering a remarkably wide range of functionalities, previously exclusive to professional SDR hardware costing thousands of dollars. It is obvious that the functionality of such amateur SDR modules cannot match the capabilities and quality of professional dedicated SDRs. However, over the years, these SDR dongles have often proved more than sufficient not just for enthusiasts, but also for demonstration purposes in complex projects. Apart from the price,

their extensive community support is another advantage, resulting in many open-source software solutions, including solutions for DoA estimation. A great overview of these devices is provided in [20]. Given the wide range of possibilities, the question arises as to which module is most suitable for the intended use. While almost every DVB-T dongle with the RTL2832U chip could serve as a suitable candidate, dongles often differ in the rest of the included hardware. A special attention should be given to the tuner, which determines the frequency range of the device. The most common tuners are R820T and its newer version R820T2, along with tuners R828D and E4000. Their differences are presented in the Table 4.1. The R828D tuner is

Tuner	Min. Freq. [MHz]	Max. Freq. [MHz]
R820T/R820T2	24	1766
R828D	24	1766
E4000	52	2200

Table 4.1: Frequency ranges of the most popular tuners.

almost identical to the R820T but is often found in lower-quality dongles despite its higher price. Conversely, the E4000 chip, while known for its superior performance, is becoming increasingly rare and expensive due to its discontinuation. For low-cost DoA estimation projects, the RTL-SDR V3 modules with the R820T2 tuner are extensively utilised, thanks to their exceptional price-to-performance ratio. This single-channel receiver offers a tunable range from 24 MHz to 2.2 GHz, a maximum baseband bandwidth of 3.2 MHz, and two 8-bit ADCs offering sampling rate up to 3.2 MS/s. Synchronisation of multiple dongles for coherent multichannel signal processing is possible, but often requires modifications of the SDR hardware. In [21][22], synchronisation is achieved using an external reference noise generator and a clock source, with reference clock signal fed directly to the dongles. Phase-locked loops are used to derive frequencies of LOs for sampling, and samples are aligned in both time and phase using cross-correlation. Alternatively, similar solution can be obtained using an off-the-shelf external timer PCB, such as the one from Coherent Receiver, as demonstrated in [23]. For applications requiring variable scaling, synchronisation using a reference signal with its source located in the far-field region is described in [24]. Finally, [25] presents a solution for synchronisation without modifying any of the RTL-SDR hardware. A wideband reference signal is supplied to a pair of antenna arrays. Frequency and time synchronisation of the received signals can then be realised with respect to this reference signal.

## **KerberosSDR and KrakenSDR**

KerberosSDR and KrakenSDR, both products of the team behind the RTL-SDR V3, were developed specifically for the purpose of coherent multichannel reception. KerberosSDR initially launched through crowdfunding and became renowned in the SDR community thanks to its DoA estimation, beamforming, and radar capabilities, which are not readily available in commercial off-the-shelf products. The architecture is based on four coherent RTL-SDRs integrated onto a single board, inheriting technical specifications from RTL-SDR V3 dongles. Time and phase synchronisation are achieved through a shared reference clock signal and generated noise signal. KrakenSDR is an updated version of Kerberos, introducing several improvements. Notably, in comparison to its predecessor, KrakenSDR increases the number of coherent channels to five, and incorporates new switching hardware to eliminate the need for manual disconnection of all antenna inputs during frequency reconfiguration and device startup to achieve optimal phase and sample calibration.

## **FunCube**

This SDR is a unique piece of hardware developed in collaboration with AMSAT's FUNCube Satellite project. Its primary purpose was to provide an inexpensive SDR dongle, operating in both the VHF and UHF bands. This enabled enthusiasts in the AMSAT community to receive signals from the FUNCube CubeSat. To date, the FUNCube project remains active, having launched a total of three CubeSats containing linear U/V transponders. The SDR was initially released in 2010, and ever since, the hardware has received minimal upgrades. There are two versions available: a basic version that allows reception of signals only within the frequencies reserved for the FUNCube mission, and a more expensive Pro version that enables reception across the entire operational range. The architecture of the FUNCube dongle is based on the E4000 tuner and the PIC24 microcontroller from Microchip Technology. While the dongle continues to be purchased by enthusiasts active in the AMSAT community, the technology is considered somewhat obsolete compared to more recent SDR devices available on the market. FunCube dongle offers a tunable range from 150 kHz to 240 MHz and from 420 MHz to 1.9 GHz, a maximum baseband bandwidth of 20 MHz, 10-bit ADC resolution, and a sampling rate of 192 kS/s.

## **AirSpy**

AirSpy offers a range of SDR single-channel receivers designed to cover the HF to UHF bands. The AirSpy Mini and AirSpy R2 SDRs are built on the R860 chip. This chip is essentially identical to the R820T2 with minor manufacturing modification



that allowed production of this chip to continue. The real advantage comes in the utilisation of more modern and powerful micro-controllers, such as R2's NXP LPC4370 with higher resolution ADC and increased sampling rates. The AirSpy Mini is a dongle alternative to the R2 model. The technical specifications of the AirSpy R2 include a tunable range from 24 MHz to 1.7 GHz, a maximum bandwidth of 10 MHz, 12-bit ADC resolution, and sampling rates up to 10 MS/s. The AirSpy Mini shares the tunable range and ADC resolution, but the maximum bandwidth is reduced to 6 MHz. A major limitation of AirSpy devices is the lack of external clock support, which prevents chaining multiple devices in series. However, time synchronisation of multiple SDRs can potentially be achieved through extensive hardware modification. A common clock signal from an external source, such as an external clock PCB or clock source, would need to be fed to each individual device. Similar to BladeRF, such a solution has not yet been verified and would require thorough testing.

#### 4.1.1 Chosen SDR platform

Based on all the SDRs considered in this chapter it is now necessary to pick a viable solution that will suit the needs for the demonstration of DoA estimation methods. The final parameters that are going to serve as a guideline for choosing the right platform were derived from important RFFE parameters from chapter 3.2 and from criteria defined at the beginning of this chapter. All the research from the previous section can be reduced to a singular table. Hence, the right hardware is going to be chosen based on hardware attributes summarised in Table 4.2.

The most promising solution appears to be the utilisation of multiple RTL-SDR dongles alongside external clock and noise cards from Coherent Receiver. This approach offers a blend of compact form factor and fast, cost-effective hardware scalability. A lot of research has been conducted on RTL-SDRs for coherent multi-channel signal reception, providing a solid foundation for achieving adequate system performance for DoA estimation.

However, it is important to note that this solution necessitates hardware modifications to ensure proper reference signal distribution across all dongles. Additionally, the transfer of IQ samples via USB interfaces requires careful management, potentially necessitating the use of USB hubs and custom software for sample alignment and frequency offset corrections to achieve coherence.

Given the need to minimise or ideally eliminate the need for hardware interference due to limited scale of this research, the decision has been made to opt for the KrakenSDR platform, complemented by a set of five monopole whip antennas, which are usable from 100 MHz to 1 GHz. The hardware is shown in Figure 4.1.








SDR Type		Frequency range [MHz]	Baseband bandwidth [MHz]	ADC Resolution	Sampling rate [MS/s]	Noise figure [dB]	Multi-channel coherence	Price [\$]
USRP X300		DC - 6000	160	14-bit	200	<5	Yes	7825
PlutoSDR		325 - 3800	20	12-bit	65.1	<3 dB	Solution available	235
HackRF One		1 - 6000	20	8-bit	20	<4 dB	Solution available	340
BladeRF 2.0 xA4		47 - 6000	56	12-bit	61.4	<6 dB	Not tested	540
RTL-SDR V3		0.5 - 1766	3.2	8-bit	3.2	<4.5 dB	Solution available	25
KrakenSDR		24 - 1700	3.2	8-bit	3.2	<5 dB	Yes	500
FunCube SDR Pro		0.15 - 240; 420 - 1900	20	10-bit	0.192	<5.5 dB	Not tested	155
AirSpy Mini		24 - 1700	6	12-bit	6	<4 dB	Not tested	120

Table 4.2: Overview of all important parameters of considered SDRs.

KrakenSDR offers its own open-source DSP web application tailored to showcase its DoA estimation capabilities. Furthermore, an Android application can be used in parallel with the processing software to localise RF sources within the area of interest. Nonetheless, the DSP software will require modifications to enable implementation and analysis of the proposed DoA estimation methods outlined in chapter 2.



Fig. 4.1: KrakenSDR with 5 monopole whip antennas.

## 4.2 KrakenSDR setup

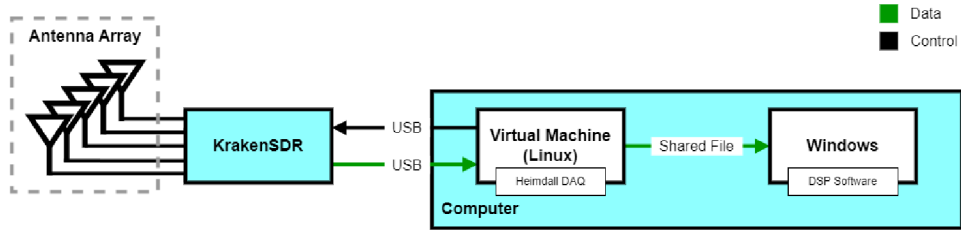
### 4.2.1 Hardware solution

The software architecture of KrakenSDR is divided into two subsystems: the Data Acquisition (DAQ) Subsystem, responsible for IQ sample acquisition and channel synchronisation, and the DSP Subsystem, which hosts a web server with GUI, providing DoA estimation and other signal processing functions. These subsystems can either operate on a single machine, sharing data through shared memory, or they can operate remotely, sharing data via a gigabit Ethernet connection.

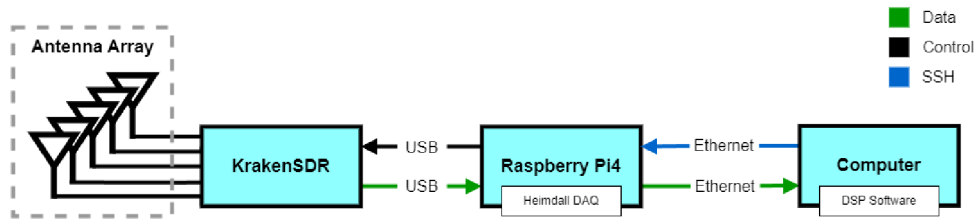
Running both subsystems on a single machine increases the hardware compactness, but deploying the DSP subsystem on a remote, more powerful machine has the potential to increase the processing throughput and ensure higher system stability. To achieve the highest possible throughput and enable real-time processing, it is advised to perform the DSP on a machine with sufficient processing capacity.

Two setups were initially tested. In the first setup, KrakenSDR was directly connected to a PC via USB-C interface. The computer ran both DAQ and DSP software on a Linux virtual machine (VM), with system image downloaded from the

hardware provider’s website. The block diagram of this setup is illustrated in Figure 4.2a.



(a) DoA estimation setup through virtual machine.



(b) DoA estimation setup through Raspberry Pi.

Fig. 4.2: Presented KrakenSDR configurations.

The setup initially appeared to function adequately with provided DSP software. However, issues arose when attempting to replace the DSP software with a custom solution. The VM proved to be unstable and slow, even with increased RAM allocation. It is believed that improvements in speed could be achieved by additional tweaking the allocated resources and running the custom DSP software within the virtual environment. Nonetheless, such a setup was undesirable as the author was most familiar with the Windows operating system.

There was lack of reliable solution for transferring data from the VM to Windows. Initially, it was thought that the DAQ software could dump the data into a file located in a folder shared between the virtual machine and the PC itself. However, this data transfer method slowed down the processing even further. The final solution involved recording a data sample stream via GNU Radio Companion on the VM and then extracting this file from the shared folder in Windows. Unfortunately, this only allowed for retrospective data analysis. It was also discovered that the USB interface achieves acceptable throughput only at distances of less than 8 meters.

Given these restrictions, it seemed more worthwhile to investigate the potential of directly running the DSP software on Windows. After multiple failed attempts, a final working setup was created, enabling direct signal processing on a Windows PC. The diagram is illustrated in Figure 4.2b.

Here, the Raspberry Pi (RPI) is running the DAQ software and acquired data is forwarded to the Windows PC via gigabit Ethernet. The computer connects to the RPI via SSH, facilitating remote control of the hardware. The gigabit Ethernet enables significantly higher throughput over long distances compared to the USB interface. As a result, this configuration enables the KrakenSDR and RPI to be housed separately at distances up to hundreds of meters.

### 4.2.2 Software solution

The hardware requires custom software solution to facilitate data transfer from KrakenSDR to the DSP application running on the PC. The RPI's SD card is flashed with a non-desktop Linux image available from the KrakenSDR website, configured to run the DAQ software and the web-based DSP processing application. The objective is to forward IQ data samples from the DAQ software via Ethernet for subsequent DSP. The DAQ settings are adjusted to direct IQ data immediately to the Ethernet port rather than shared memory.

The volume of data generated by the DAQ software, particularly with all five channels active, is quite substantial. Data streaming over WiFi proved inadequate in delivering the required data rate, creating a substantial bottleneck in the processing chain. While LAN network connection generally provided acceptable data rates, but occasional bottlenecks arose due to multi-point switching, leading to system unreliability. To address these problems while maintaining high data rate, a direct point-to-point connection between RPI and the PC is recommended, offering the most reliable solution.

Two methods for accessing the RPI's terminal were explored, both requiring SSH to be enabled on the Raspberry computer. The first method involved connecting the RPI to a WiFi network immediately on boot. This allowed the RPI to maintain internet access, enabling software updates through the terminal accessed via a PC using a terminal emulator application (such as "Putty"). While internet access may be practical for the final deployment, it is not critical for this research as no adjustments to the software running on the RPI are necessary. The second method enables access to the RPI's terminal through a point-to-point Ethernet connection via SSH, reducing the setup's complexity by eliminating the need for WiFi. This has proven to be the best option as it enables quick deployment in testing without dependence on accessible WiFi networks.

On the PC, the DSP is accomplished through a GNU Radio Companion app with KrakenSDR's out-of-tree signal processing extension or a custom Python application. A comprehensive tutorial for configuring the testing setup is provided in [26].

The GNU Radio setup is very straightforward. The KrakenSDR source outputs raw IQ samples, which are then directly fed into file sink blocks, writing the data from each channel into separate text files in a chosen directory. The GNU Radio block diagram is displayed in Figure 4.3. The QT GUI sink blocks are optional and are used for displaying frequency spectra of signals on individual channels. This can be useful especially when checking for in-band interference.

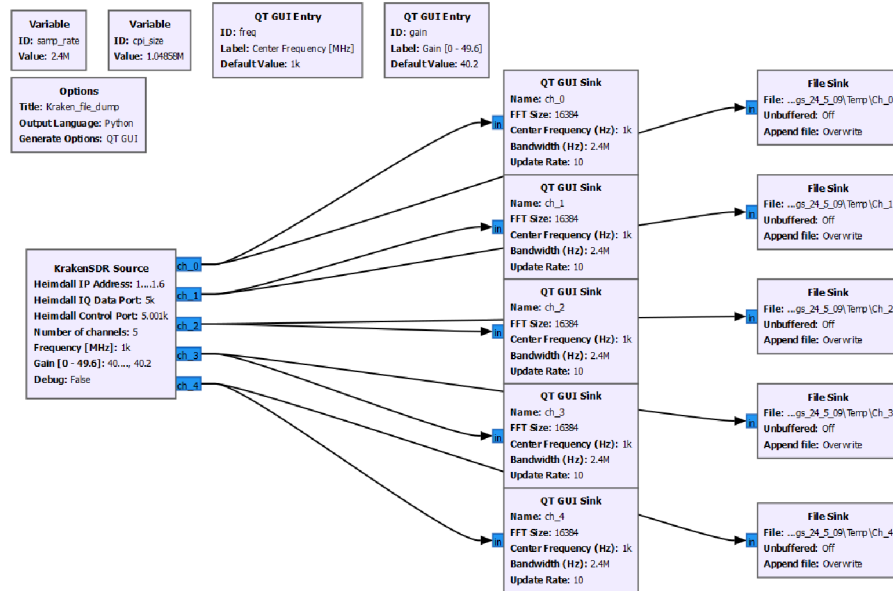


Fig. 4.3: GNU Radio block diagram for recording of IQ samples.

The KrakenSDR source block is a powerful tool that ensures connection, system initialisation, parameter reconfiguration, and extraction of IQ data samples. Therefore, it serves as an excellent foundation for any custom DSP application, as communication with the Heimdall DAQ software does not need to be designed from scratch. Designing such a system would require extensive dissection of the DAQ software, which is not feasible for research of this scale. The custom DSP application was created by modifying the KrakenSDR source block class available on the KrakenSDR GNU Radio GitHub web page.

The source block obtains IQ data samples from an IQ header and inserts them into a queue. Multi-threaded processing is implemented, which is necessary for correct integration into the GNU Radio application. The work function then extracts IQ samples from the queue and forwards them to the output. This sample forwarding is orchestrated by GNU Radio's scheduler and framework, which handles the implementation and connection of the signal processing blocks by calling the work function when the blocks further down the processing chain are ready to acquire more samples. Therefore, the work function sample forwarding does not operate outside the GNU Radio ecosystem.

In the custom solution, the work function is replaced by a function that directly accesses IQ samples from the buffer and immediately performs DoA estimation calculation based on the chosen estimation technique. This solution has proven effective for processing the IQ samples in real-time and continues to work even if the estimation calculation is too slow to keep up with the queue. In such cases, leftover samples are dropped until all calculations have been performed and a new spot in the queue becomes available.

# 5 Array and DoA estimation performance analysis

## 5.1 Array pattern analysis

The antenna pattern can be theoretically approximated by Bartlett's beamformer. The spatial spectrum derived from the estimation can be used to visualise the pattern. When simulating an impinging signal arriving from an arbitrary angle, aligned with the desired steering direction of the array, a comprehensive scan of the range of interest allows the spatial spectrum to emulate the array's radiation pattern accurately. However, in practice, the pattern is computed by summing the contributions of individual omnidirectional elements within the array across a predefined angular range. The resulting pattern displays array's directivity, which is normalised to represent a generalised scenario.

### Number of elements

The influence of increasing the number of elements in the array was investigated through the simulated array pattern. Inter-element spacing was set to  $0.5\lambda$ , with elements having uniform gain distribution across the array. No array steering was applied. Results are displayed in Figure 5.1 for various numbers of array elements.

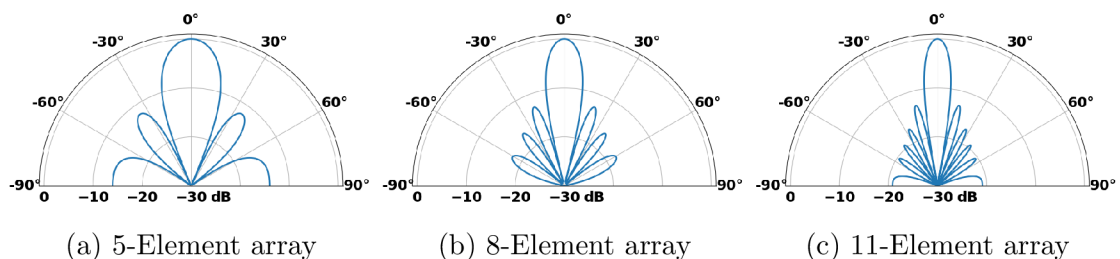


Fig. 5.1: Normalised ULA pattern based on the number of array's elements.

As the number of elements increases, the width of the main lobe decreases, while the number of side lobes increases. Consequently, the side lobe power is distributed more equally into undesired directions, which increases the main lobe to side lobe power ratio. In conclusion, an increased number of elements narrows the main beamwidth and enhances the resolution of DoA, as power contributions from undesired angles are increasingly suppressed with the number of elements. However, this increase in array size with each added element increases the required computational throughput, overall cost, and array size.



## End-fire distortion

It is expected that the resolution of the array decreases as the scan angle approaches the array's end-fire directions. The differences between phases become less significant as the derivative of the spatial frequency function decreases as angle  $\theta$  approaches 90 degrees. The effects of the scan angle on the DoA resolution are shown in Figure 5.2. An 8-element array, with inter-element distance of  $0.5\lambda$ , is scanned from array's boresight to the end-fire.

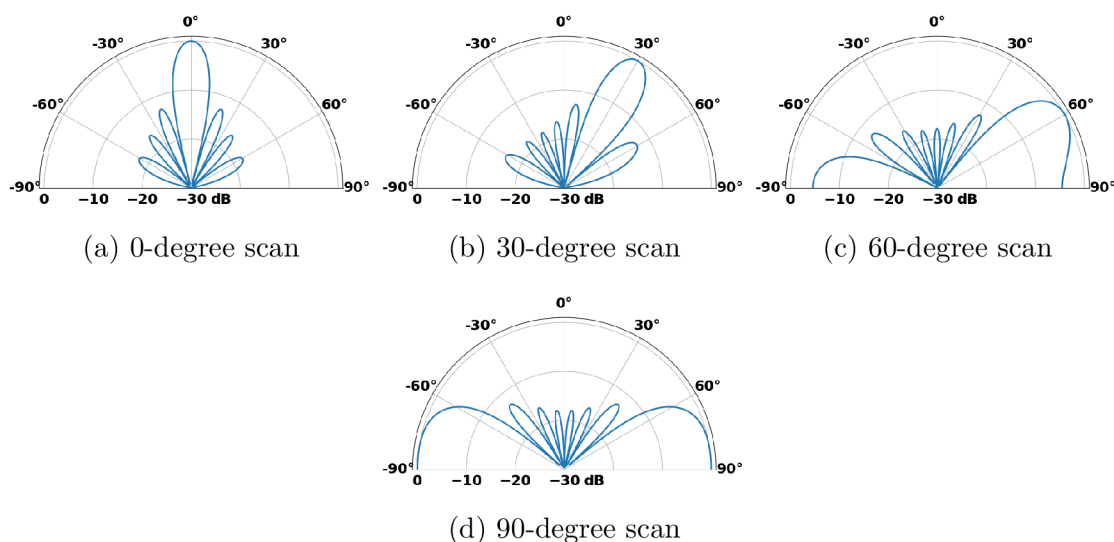


Fig. 5.2: Normalised ULA pattern based on the scan angle.

In the presence of two signals impinging the array close to end-fire, the decreased resolution results in lower accuracy. The usable scanning range for DoA estimation, where these effects remain minimal, is generally considered to be from  $-60$  to  $+60$  degrees.

## Inter-element distance

An 8-element antenna array steered to 10 degrees from the array's boresight, had its inter-element spacing adjusted from  $0.5\lambda$  to  $2.5\lambda$ . Resulting array patterns are provided in Figure 5.3.

Increasing the distance between elements beyond  $0.5\lambda$  results in spatial aliasing, which causes the formation of grating lobes, thereby generating spurious responses at unintended angles. This spatial aliasing effect can be explained by the Nyquist Sampling theorem. To correctly translate a signal into a frequency domain, two samples per period of the highest harmonic component of the signal are required. Similarly, for spatial domain, there must be at least two elements per wavelength to

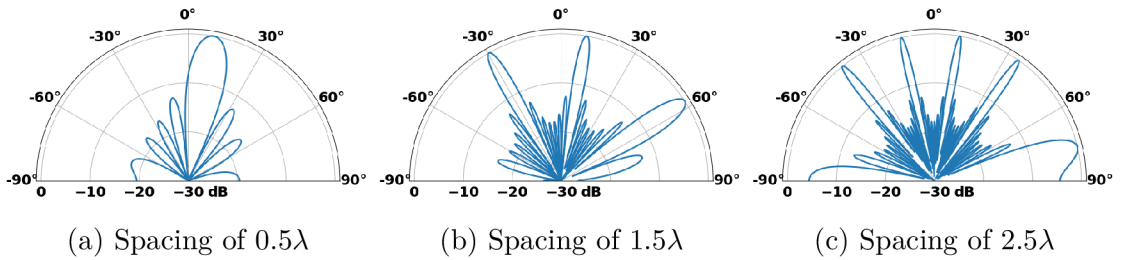


Fig. 5.3: Normalised ULA pattern based on increasing inter-element distance.

avoid the repetition of the spatial spectrum, which reduces the available scanning range.

As the inter-element distance increases beyond half of the wavelength, the available scanning range gets reduced, but the beamwidth of the main lobe decreases. The narrower beamwidth be advantageous for increasing the precision of DoA estimation algorithms, albeit at the cost of scan range reduction. This trade-off is particularly useful in situations where the scanning range is not required to span the entire 180 degrees. Nevertheless, it should be noted that the larger inter-element spacing also increases requirement on the array size.

To investigate effects of reduced inter-element spacing, the same array configuration was employed, with spacing adjusted from  $0.5\lambda$  down to  $0.1\lambda$ . Array patterns are displayed in Figure 5.4.

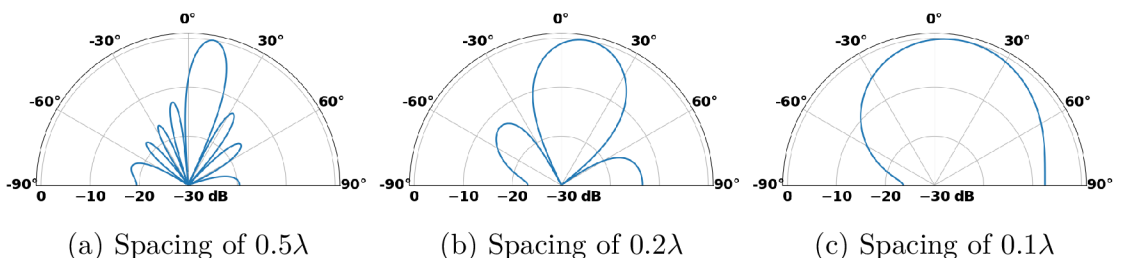


Fig. 5.4: Normalised ULA pattern of based on decreasing inter-element distance.

As the inter-element spacing is reduced, the main lobe beamwidth increases, thereby reducing the resolution of DoA estimation. This limitation is particularly restricting when multiple signals impinge the array from closely spaced angles. However, in space-constrained environments, the reduction in inter-element spacing allows for smaller array footprint at the cost of DoA estimation resolution.

## Spatial tampering

Spatial tampering is a technique employed in numerous DoA estimation methods to enhance the quality of the results by modifying the gain distribution across array elements. This gain variation is achieved through introduction of scalar weights that multiply the input data from individual channels. The technique is integral to weighted estimation algorithms such as linear prediction or minimum norm MUSIC. The effects of spatial tampering on the array pattern were investigated by applying various window functions to add weights to the input data streams. Simulations were conducted using an 8-element array, with a fixed inter-element spacing of  $0.5\lambda$  and no steering applied. The resulting array patterns are depicted in Figure 5.5.

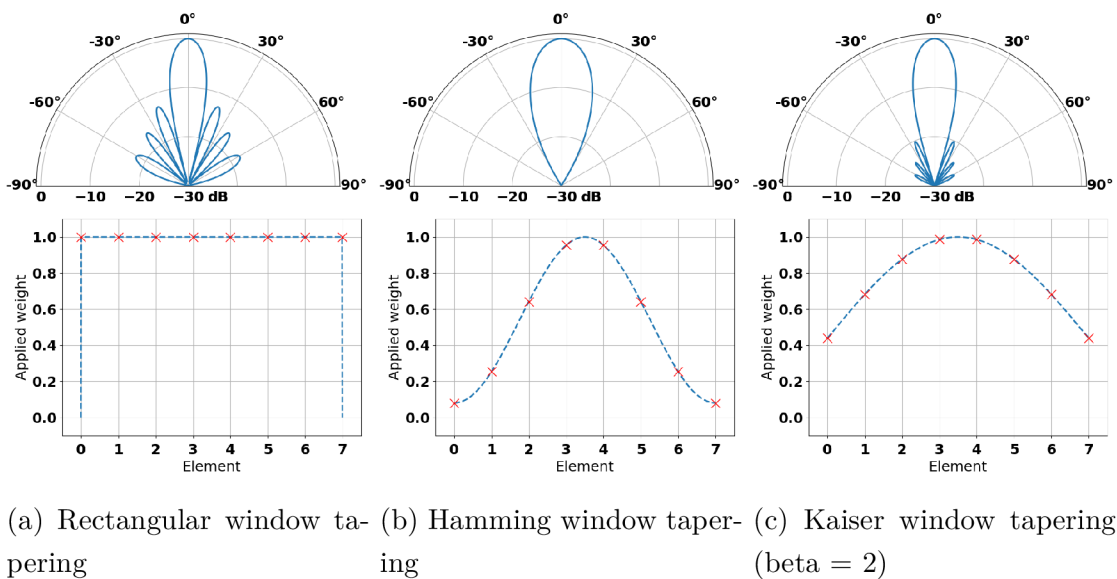


Fig. 5.5: Normalised ULA pattern with spatial tampering using windowing functions.

Selecting an appropriate weight distribution can result in suppression of side lobes, thereby reducing power contributions from undesired directions at the expense of overall gain reduction. This reduction in gain, however, reduces accuracy in environments with low SNR. Furthermore, tapering increases the main lobe beamwidth. A compromise must be found between suppressing contributions from undesired directions and maintaining a narrow beamwidth.

## 5.2 DoA estimation performance for ULA

DoA estimation techniques were applied to an artificial data sample. The generated signals impinging on the array are complex harmonic signals. Data on each element

is obtained by multiplying the incoming signal with adequate phase shifts, corresponding to the phase shift induced by the additional distance between the first and the  $n$ -th element. Additive white Gaussian noise is added to each channel separately. The data matrix thus corresponds to the equation 1.10, and the covariance matrix is obtained from 2.4.

The performance of DoA estimation techniques was assessed based on four metrics:

- Resolution: The ability of a technique to resolve closely spaced sources.
- Robustness: The ability of a technique to operate in a low SNR environment and in the presence of coherent signals.
- Computational complexity: The execution time for each algorithm.

The analysis was performed on Beamforming and Subspace-based algorithms discussed in chapter 2. The spatial spectrum calculations were carried out over a range from  $-90$  to  $90$  degrees. The accuracy of the techniques was determined by calculating the root mean square error (RMSE) between the true and estimated values. All simulations were conducted using a 5-element ULA with inter-element spacing of half wavelength, with an assumption that the number of impinging signals was known, matching the configuration used in the practical measurements. Simulation results can thus be compared to the subsequent measurement results. Beamforming and subspace-based methods are analysed separately for increased clarity. Throughout the analysis, the linear prediction technique had the unity set to position zero, i.e. the first element of the array.

## Resolution

Resolution analysis was performed by generating two equally powered, non-coherent, single-tone signals impinging on the ULA from angles  $\theta_1 = 10^\circ$  and  $\theta_2 = 40^\circ$ , with an assumed SNR of 20 dB. The spatial spectrum for the initial angles is shown in Figure 5.6.

The resolution of individual techniques was determined by reducing  $\Delta\theta = \theta_2 - \theta_1$ . The RMSE was calculated and graphed against  $\Delta\theta$ . Results are displayed in Figure 5.7.

The RMSE for the Bartlett's estimation technique has the poorest resolution of all proposed algorithms, as there is a sharp increase of RMSE already at  $\Delta\theta \approx 23^\circ$ . This originates from the fact that the beamwidth of the main lobe of a 5-element ULA is quite large. Therefore, when performing the Bartlett's estimation, the resulting values at scanned angles include substantial power contributions from all directions covered by the main lobe, requiring significant angular separation to provide accurate DoA estimates. The accuracy of MVDR starts to drop at around

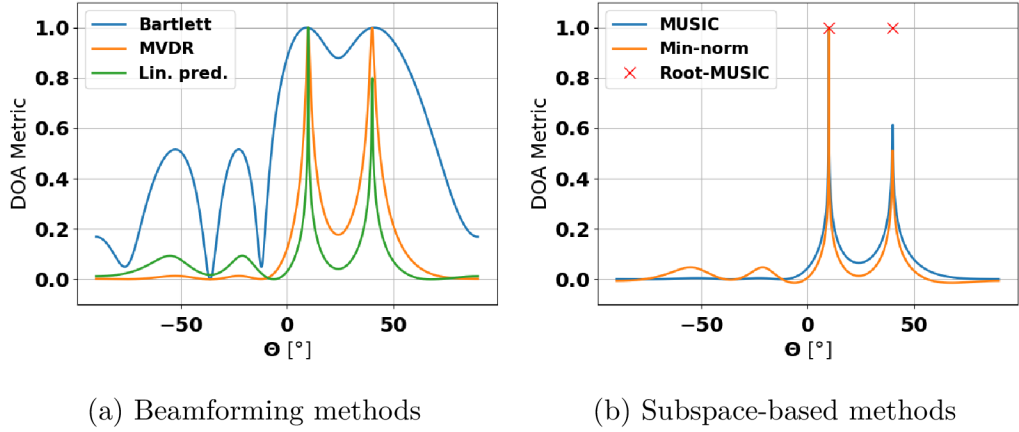


Fig. 5.6: Spatial spectra of DoA estimation techniques for  $\theta_1 = 10^\circ$  and  $\theta_2 = 40^\circ$ .

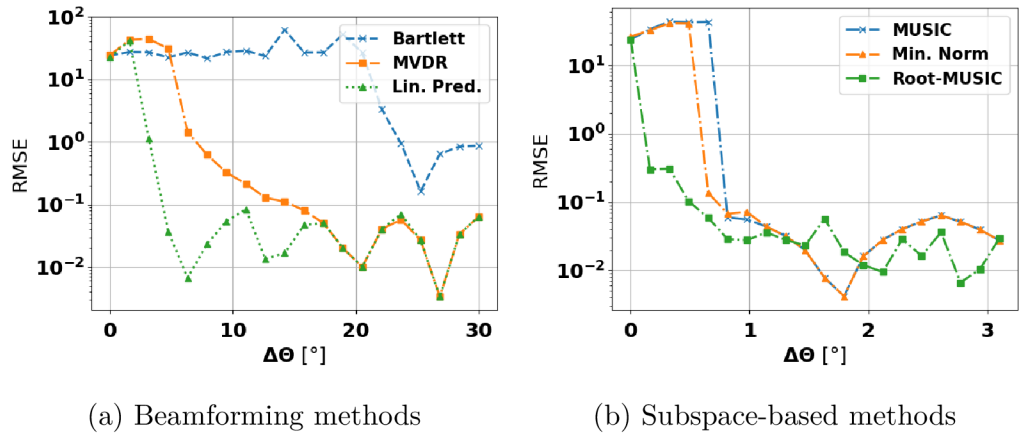


Fig. 5.7: RMSE of DoA estimation techniques based on  $\Delta\theta$ .

$\Delta\theta \approx 15^\circ$ . This method also reduces the spectrum variability at angles other than those related to the directions of impinging signals, essentially smoothing it out. The linear prediction method offers the highest resolution out of all beamforming methods, with a sharp decrease in accuracy around  $\Delta\theta \approx 5^\circ$ . While being more accurate than MVDR, the method exhibits higher spectrum variability.

All subspace-based methods outperform beamforming methods in accuracy at low  $\Delta\theta$ . Therefore, their resolution capabilities were closely investigated for  $\Delta\theta < 3.1^\circ$ . The MUSIC and Min-norm algorithm fail at around  $\Delta\theta \approx 0.7^\circ$ . The Root-MUSIC consistently achieves low RMSE across the entire range of  $\Delta\theta$ , demonstrating excellent resolution capabilities, with a sharp decrease in resolution at around  $\Delta\theta \approx 0.5^\circ$ .

## Robustness

To analyse the robustness of individual techniques, the effects of decreasing SNR on the accuracy of DoA estimations were investigated. A singular signal was generated, impinging on the array from angle  $\theta = 20^\circ$ , with SNR decreasing from 25 dB down to -25 dB. The RMSE plotted against decreasing SNR levels for all techniques is graphed in Figure 5.8.

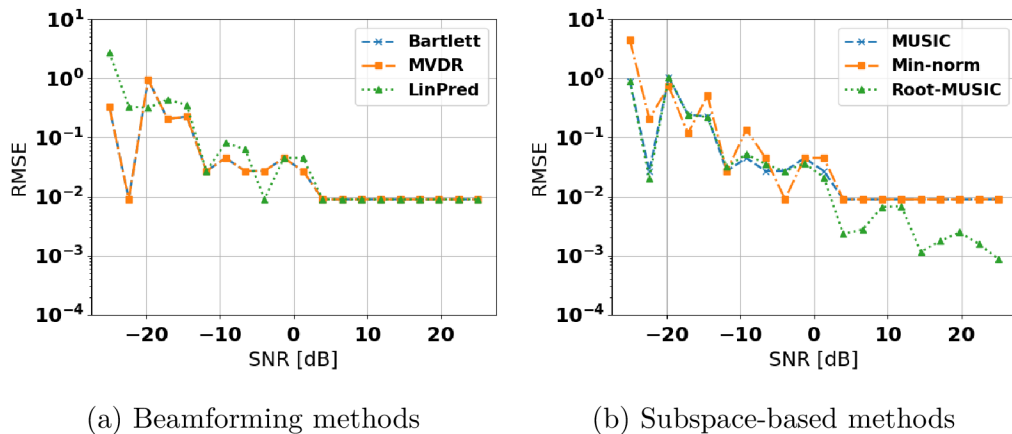


Fig. 5.8: RMSE of DoA estimation techniques based on SNR.

The figure indicates that all methods experience similar decrease in accuracy in low SNR environment. It is known that subspace-based methods should be outperformed by beamforming methods, as the differentiation between the noise and signal subspaces becomes challenging at low SNR levels. However, the single-tone signal seems to possess characteristics that are favourable for both beamforming and subspace-based methods and hence the difference is not so eminent. Ideal single-tone signals are typically simpler to estimate, leading to similar performance across different methods.

The robustness of techniques was also analysed in terms of coherent signals. DoA estimation of two highly coherent signals with a common frequency impinging the ULA from angles  $\theta_1 = 10^\circ$  and  $\theta_2 = 40^\circ$  was performed through all techniques. The SNR was kept at 20 dB. Resulting spatial spectra are shown in Figure 5.9.

The presence of coherent signals affects the accuracy of both beamforming and subspace-based techniques. Beamforming techniques experience a decrease in accuracy by around  $20^\circ$ , with the exception being the linear prediction, which remains unaffected. The accuracy of the linear prediction technique depends on which element is set to unity. Best results are obtained when the first or last elements are chosen. Bartlett's and MVDR techniques experience spatial spectrum smearing as power contributions of two coherent signals overlap. Due to power contribution from

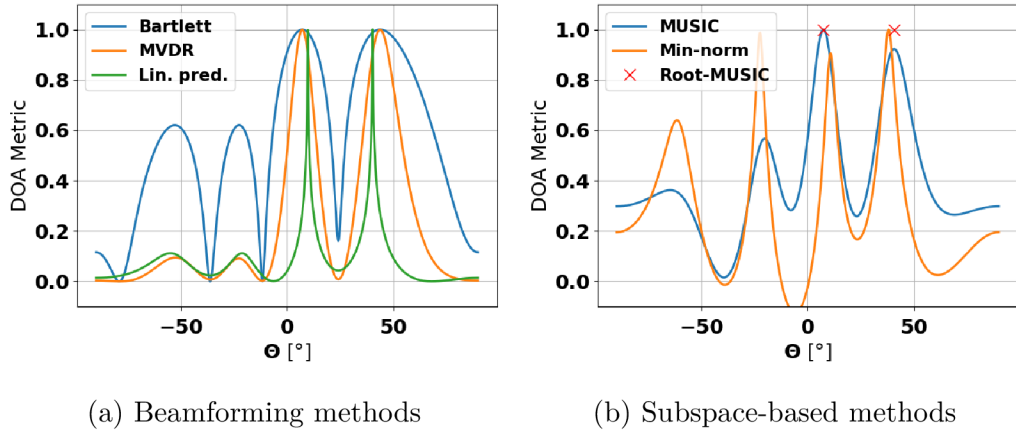


Fig. 5.9: Spatial spectra of DoA estimation techniques in the presence of two highly coherent signals.

side lobes, the DoA metric maximum shifts towards the direction of the other coherent signal. This shift is dependent on multiple factors such as the array pattern, signal power, and direction.

MVDR and linear prediction techniques are expected to fail in the presence of purely coherent signals due to inverse matrix multiplication. The noise aids in the differentiation of the signals by disrupting their coherent patterns, making it easier to identify individual signal characteristics. If no noise is present, these algorithms fail completely, as can be seen in Figure 5.10.

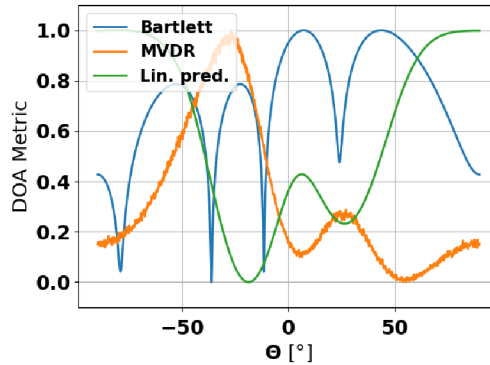


Fig. 5.10: Spatial spectra of Beamforming DoA estimation techniques in the presence of two highly coherent signals with no noise present.

Subspace-based methods fail completely as they rely on the distinct separation of signal and noise subspaces. In the presence of two or more coherent signals, the signal covariance matrix is not full rank. The presence of noise does not improve accuracy as its decorrelation effects do not provide enough resolution for correct subspace

decomposition. The employment of preprocessing methods successfully decorrelates the signal covariance matrix and makes the subspace-based methods usable even in the presence of coherent signals. The effects of preprocessing techniques are displayed in Figure 5.11.

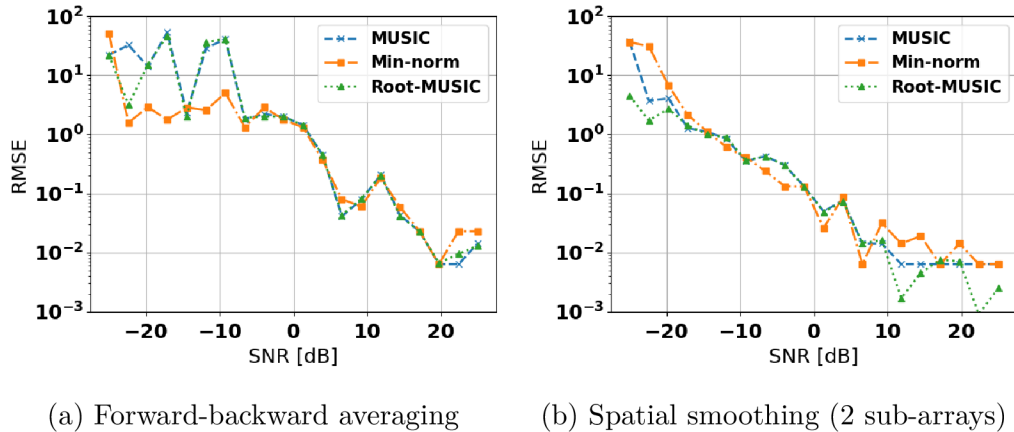


Fig. 5.11: Effects of preprocessing methods on DoA estimation techniques with decreasing SNR.

Although the techniques do not experience degradation in accuracy at high SNR, the effects on accuracy become evident as SNR decreases. Figure 5.11 shows an increase in RMSE at much higher SNR levels in comparison to Figure 5.8. The accuracy starts to decrease at around 12 dB SNR for forward-backward averaging and around 7 dB SNR for the spatial-smoothing method.

## Computational complexity

The computational complexity was estimated by measuring code execution time for each technique using Python's time library. DoA estimation was done by generating a million I/Q samples for each channel, with the spatial spectrum range split into ten thousand angular samples. For subspace-based methods, model order estimation is required before DoA estimation. However, model order estimation does not have to be performed continuously. Instead, this estimation can be performed at the initialisation and then performed at a specified interval dependent on the expected changes depending on the environment. In addition, post-processing to determine peaks in the spectrum was performed and the focus was put purely on the estimation techniques, with each technique performed once. Resulting code execution times are displayed in Table 5.1.

The Root-MUSIC technique outperforms all other techniques listed. This aligns with the theory, as the estimation of roots of the Root-MUSIC polynomial should



Estimation technique	Code execution time [ms]
Bartlett beamformer	198.2
MVDR	210.1
Linear prediction	242.9
MUSIC	210.7
Minimum norm	309.0
Root-MUSIC	44.0

Table 5.1: Approximate code execution times for various DoA estimation techniques.

deliver increased computational speeds if implemented correctly. NumPy’s root estimation function, required for the polynomial estimation, appears to be well-optimised. Direct calculation is always expected to be faster than scanning the angular range of interest, which must be divided into enough angular samples to provide decent resolution. Bartlett is the second fastest algorithm, as it does not require additional calculation on inverse matrices or eigenvalue decomposition. Nevertheless, the reduction of processing time of the Bartlett algorithm is quite insignificant in comparison to all other techniques outside Root-MUSIC, with their processing times fluctuating around 210 to 280 milliseconds.

### 5.3 DoA estimation performance for UCA

Lastly, a brief investigation was conducted for a UCA setup that in theory shall enable DoA estimation over the entire azimuthal range, from -180 to 180 degrees. In addition, the 3-dimensional configuration enables estimation of the elevation angle. This, however, comes at a significant increase in computational complexity as for each azimuthal angle, a scan from 0 to 90 degrees is required. A single tone harmonic signal was simulated to impinge a 5-element UCA with inter-element spacing of  $0.5\lambda$  under azimuth  $\theta = 25^\circ$  and elevation  $\phi = 15^\circ$  with  $\text{SNR} = 20$  dB. The DoA estimation was performed using adapted Bartlett, MVDR, and MUSIC estimation techniques. Spatial spectra of these methods are shown in Figure 5.12.

These DoA estimation techniques have proven to be directly adaptable from ULA to even more complex array structures, as long as the inter-element phase relations are correctly modelled. Performance of UCA was assessed with decreasing SNR levels. The resulting RMSE is displayed in Figure 5.13.

In comparison to ULA, the resolution of estimation algorithms for UCA starts to decrease at around 2 dB SNR. The performance of MVDR is notably decreased in comparison to ULA. The UCA’s beam pattern has higher side lobe levels, making

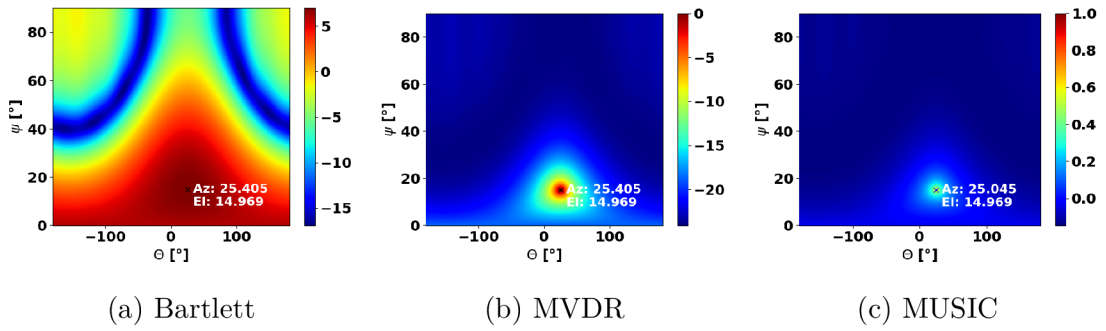


Fig. 5.12: Spatial spectra of DoA estimation techniques for UCA configuration.

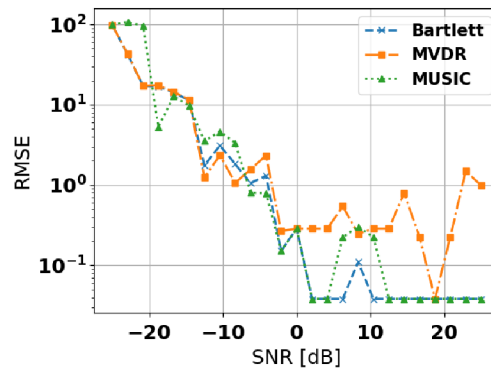


Fig. 5.13: RMSE of DoA estimation techniques based on SNR for UCA configuration.

it more susceptible to noise and interference.

## 6 Practical verification of DoA estimation methods

The main goal of the practical measurement is to validate the DoA estimation capabilities of the SDR hardware in combination with experimental software configuration. The measurement setup should simulate an environment with no multi-path propagation. A signal transmitted from the source is expected to travel directly to the array and impinge only from the source's direction. To meet the requirements for minimising multi-path propagation, measurements can either be conducted in an open field, far from any obstacles that could reflect the signal, or in an electromagnetically shielded chamber, where the effects of multi-pathing are greatly suppressed.

### 6.1 Proposed measurement setup

To suppress the effects of multi-pathing and outside interference, the measurements were performed in the anechoic chamber located in the electromagnetic compatibility laboratory at Brno University of Technology. An anechoic chamber is an enclosed room with walls made of steel plates, ensuring electromagnetic tightness, and is designed to operate across a frequency range from 10 kHz to around 10 GHz. The chamber provides external interference attenuation from 80 to 120 dB. The chamber's walls are covered with absorbing material, which reduces the wall reflection coefficient to a minimum, to suppress the effects of internal reflections.

The setup was proposed based on restrictions imposed by the KrakenSDR antenna limitations and the parameters of the anechoic chamber. The most important parameters are listed in Table 6.1.

Size (L x W x H)	7.05 x 4.05 x 3.075 m
Frequency range	10 kHz to 10 GHz
External interference attenuation	100 dB

Table 6.1: Anechoic chamber parameters.

KrakenSDR was positioned inside of the chamber along with a signal generator. It is crucial to consider the influence of the distance between the receiver and the transmitter. Due to the irregularity and partial unpredictability of the pattern in the near-field, the measurements were realised in the far-field, where the pattern characteristics become more stable. Given the chamber's small dimensions, the frequency of the impinging signal was set to the maximum allowed by the hardware

to ensure that the far-field region could be considered at a short distance. The frequency of the impinging signal was set to 1 GHz, which is the maximum frequency for which KrakenSDR's extendable whip antennas are designed.

The required length of whip antennas is obtained as for any other monopole:

$$\lambda = \frac{c}{f} = \frac{3 \cdot 10^8}{1 \cdot 10^9} = 0.3 \text{ m}$$

$$L = \frac{1}{4}\lambda = \frac{1}{4} \cdot 0.3 = 0.075 \text{ m} = 7.5 \text{ cm}$$

This length is achieved when antennas are completely collapsed, which is beneficial as it is often difficult to achieve identical extension of individual segments on all whip antennas for a desired frequency. Therefore, collapsed antennas increase the reproducibility of measurements.

The inter-element spacing  $\Delta$  is set to half the wavelength to maintain the full spatial spectrum resolution range, without the effects of grating lobes. In such case, the total size  $D$  of a 5-element ( $m = 5$ ) ULA is calculated as:

$$D = (m - 1)\Delta = (m - 1)\frac{\lambda}{2} = (5 - 1)\frac{0.3}{2} = 0.6 \text{ m}$$

The required minimal distance between the source and the 5-element antenna array is:

$$d = \frac{2D^2}{\lambda} = \frac{2 \cdot 0.6^2}{0.3} = 2.4 \text{ m}$$

Measurements were performed using the proposed signal processing setup from chapter 4.2. The setup can be reproduced by following the guide available in [26]. A Raspberry Pi, KrakenSDR, and antennas were laid out on a wooden table at one end of the chamber. An Ethernet cable was routed via a supply opening, connecting the Raspberry Pi to a PC outside of the chamber. The signal generator, along with an antenna, was placed at the opposite end of the chamber. Cardboard boxes were used as a stand to lift the source antenna above the ground. Absorbers were then distributed covering the path from source to the receiving array to mitigate the effects of ground reflections. SNR was measured with an additional antenna connected to a spectrum analyser outside of the chamber via a coaxial feed-through. The list of used devices is given below:

- KrakenSDR + KrakenSDR whip antenna set
- Raspberry Pi 4B
- Keysight N9310A RF Signal Generator + Monopole antenna
- Rohde & Schwarz ESU40 EMI Test Receiver

The proposed measurement setup is illustrated in Figure 6.1 along with an image of the real setup in Figure 6.2.

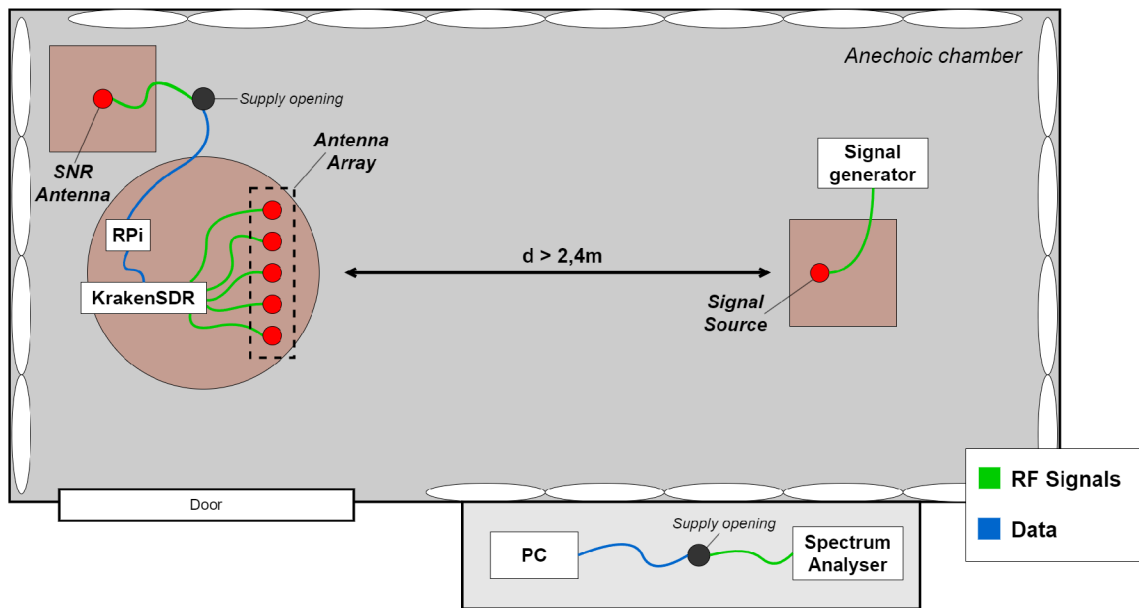


Fig. 6.1: Proposed measurement setup

The configuration of the KrakenSDR and the signal generator remained mostly the same for the duration of the entire measurement, except for changes in the amplitude levels of the generated signal. Amplitude was adjusted to decrease the SNR to assess the robustness of individual estimation techniques. Only a single-tone harmonic signal was considered to best match the simulations performed in the previous chapter. The KrakenSDR configuration can be found in Table 6.2.

Parameter	Value
Centre frequency	1 GHz
Uniform gain	40.2 dB
Number of active channels	5
Inter-element spacing	0.15 m

Table 6.2: KrakenSDR configuration for the first experiment.

## 6.2 DoA estimation measurements

For each measurement, a 15-second recording was performed using the GNU Radio Companion. Data streams were saved to separate files, which were subsequently processed in Python. The spatial spectrum calculations were performed over the full range from -90 to 90 degrees. Overall, three measurements were performed. First, DoA estimation of a single source was conducted to verify the functionality of the

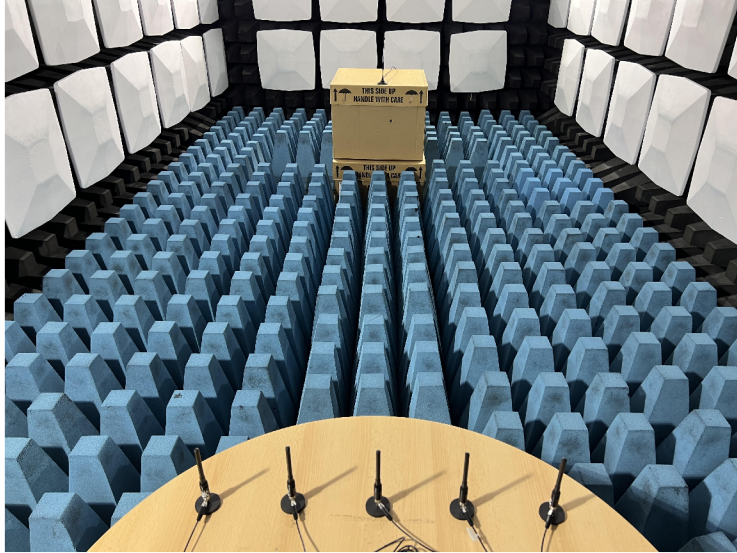


Fig. 6.2: Image of the deployed setup in the anechoic chamber.

proposed setup. Next, the performance of DoA estimation algorithms was assessed based on decreasing SNR levels. Lastly, the DoA estimation of two coherent sources impinging on the array was performed to assess the effectiveness of preprocessing techniques.

### 6.2.1 Verification of functionality

The correct implementation of DoA estimation algorithms to successfully determine the DoA of impinging signals was verified using a simple setup. Algorithms were tested with the signal source initially positioned at the array's boresight ( $\theta = 0^\circ$ ), at a distance of 3.1 meters from the receiver. Then, the measurement was repeated for angle  $\theta = 20^\circ$ , as the position was shifted 1.2 meters to the right. The signal amplitude was set to -20 dBm on the generator. The resulting spatial spectra are displayed in Figures 6.3 and 6.4.

The order of elements in the array was reversed, which resulted in an opposite shift in angle from what was expected. This, however, did not impact the overall measurement. The spatial spectrum was flipped in processing to correctly reflect changes in the source position. The mistake was corrected in subsequent measurements by manually switching the order of elements. The performance was measured based on the accuracy of the estimated angle  $\theta_{\text{est}}$ . Individual algorithms are compared in Table 6.3 based on the absolute deviation between the estimated angles  $\theta_{\text{est}}$  and the real angle  $\theta$  calculated as:

$$\text{Absolute deviation} = |\theta - \theta_{\text{est}}|$$

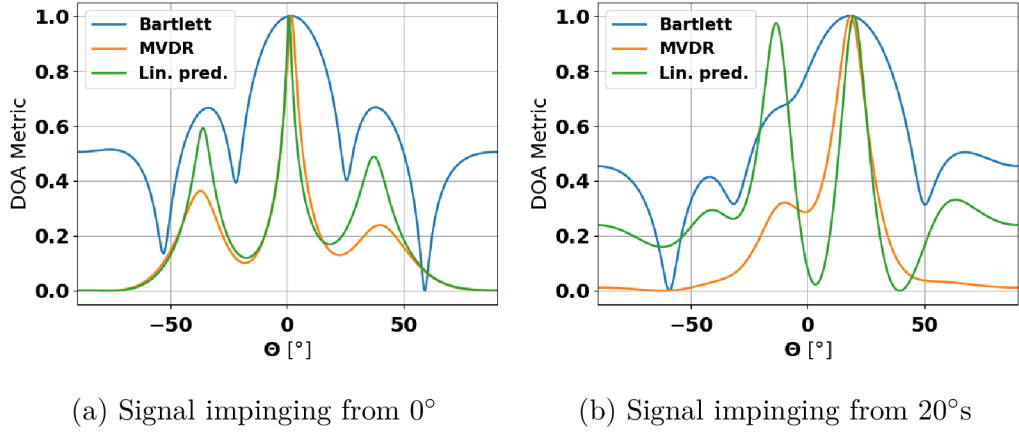


Fig. 6.3: Resulting spatial spectra of beamforming methods applied on recorded data sample.

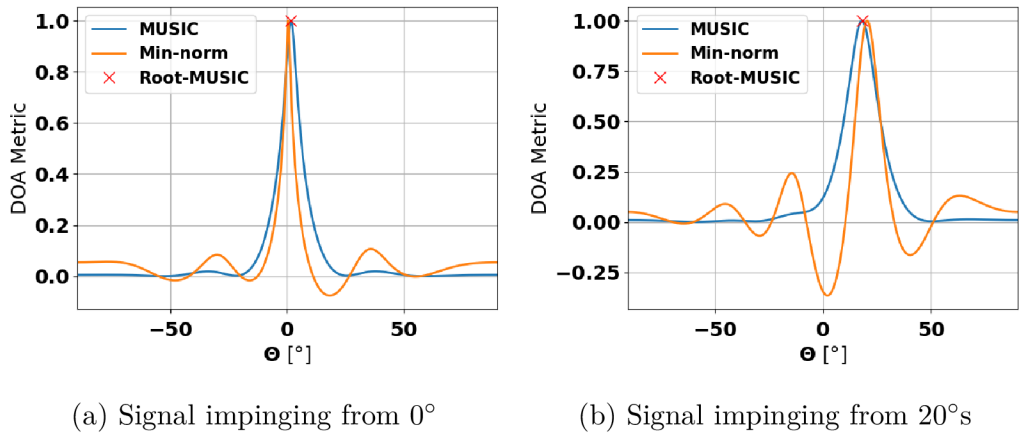


Fig. 6.4: Resulting spatial spectra of subspace-based methods applied on recorded data sample.

KrakenSDR resolution was estimated from the KrakenSDR's array size calculation sheet available from [27]. The estimated resolution defines acceptable angular offset imposed by physical hardware limitations. The hardware and the array configuration should enable DoA resolution around  $3.5^\circ$ . The measurement results show that the absolute deviation from the real angle does not exceed  $3.5^\circ$ , which indicates correct implementation of estimation algorithms. Linear prediction and min-norm algorithms exhibit significant increase in accuracy at  $\theta = 20^\circ$ . This is consistent with theory, as methods implement weights, which emphasise the largest values contributing to the estimation results. This potentially reduces the influence of noise and signal coherence. However, the success of these weighting techniques depends on many factors, including the angle of impinging signals, hence the difference

Measurement results for $\theta = 0^\circ$		Measurement results for $\theta = 20^\circ$	
Estimation technique	Absolute deviation [ $^\circ$ ]	Estimation technique	Absolute deviation [ $^\circ$ ]
Bartlett	1.712	Bartlett	1.531
MVDR	1.892	MVDR	1.892
Linear prediction	2.613	Linear prediction	0.4504
MUSIC	1.712	MUSIC	1.531
Min-norm	2.973	Min-norm	0.8108
Root-MUSIC	1.644	Root-MUSIC	1.550

Table 6.3: Performance measurements based on absolute deviation of estimation algorithms.

between  $0^\circ$  and  $20^\circ$  scenarios.

### 6.2.2 DoA estimation in low SNR environment

The robustness of estimation techniques was assessed by decreasing the amplitude of the generated signal, thereby decreasing the SNR. Initially, the amplitude was planned to be configured in relation to the SNR measured by a spectrum analyser. Unfortunately, the spectrum analyser failed to provide accurate measurements due to configuration issues. Therefore, it was decided to assess the RMSE against the amplitude configured at the signal generator.

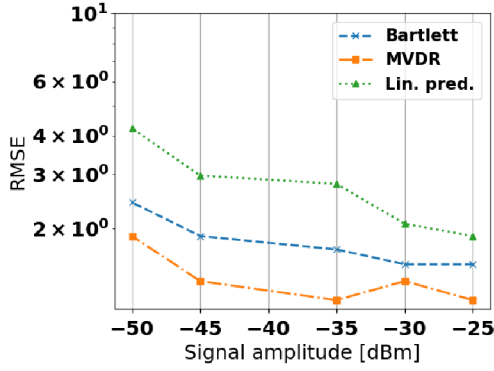
First, the signal source was positioned directly in front of the array ( $\theta = 0^\circ$ ), with a distance of 3.37 meters between the source and the receiver. Measurements were performed for signal amplitudes ranging from -20 to -50 dBm and the measurement was repeated for angle  $\theta = 45^\circ$ . Resulting RMSE values are graphed in Figures 6.5 and 6.6.

The scenario with the source positioned at angle  $\theta = 0^\circ$  shows a slow, progressive decline in the accuracy of all estimation algorithms. At angle  $\theta = 45^\circ$ , the results show a more rapid drop in accuracy of all estimation methods at signal amplitude levels around -35 dBm. The resolution is expected to drop as the angle of the impinging signal moves towards the array's end-fire direction. Therefore, the resolution decrease may become noticeable at SNR levels that are still sufficient for accurate estimation at smaller angles. In general, the beamforming methods seem to perform as well or better than their subspace-based alternatives.

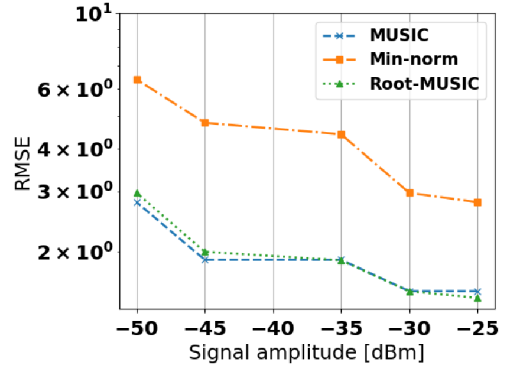
### 6.2.3 DoA estimation of two coherent signals

To enable generation of two coherent signals impinging the array from two directions, the measurement setup had to be adjusted at the signal generator end to facilitate connection of an additional antenna representing the second signal source. This was



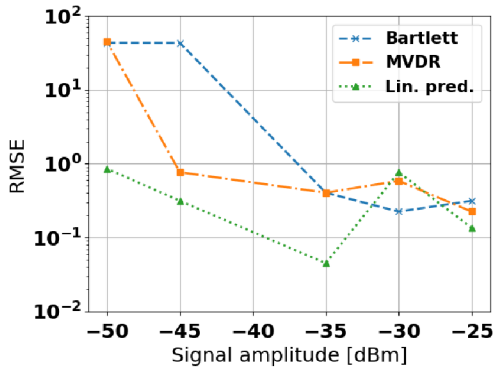


(a) Beamforming methods

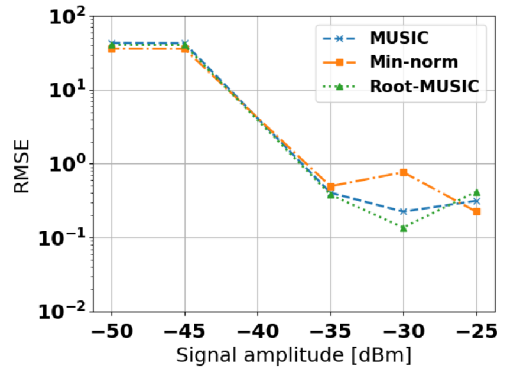


(b) Subspace-based methods

Fig. 6.5: RMSE of estimation techniques for the decreasing amplitude of the generated signal impinging on the array from  $0^\circ$ s.



(a) Beamforming methods



(b) Subspace-based methods

Fig. 6.6: RMSE of estimation techniques for the decreasing amplitude of the generated signal impinging on the array from  $45^\circ$ s.

achieved by splitting the generator's output with a simple three-way RF coaxial adaptor.

Two signal sources were initially positioned at angles  $\theta_1 = -20^\circ$  and  $\theta_2 = 5^\circ$ . The distance between the source and the receiver was increased to 3.65 meters, and the signal amplitude was set back to -20 dBm. The distance between sources was gradually decreased by reducing the angle  $\theta_2$  down to  $-15^\circ$ . The RMSE was calculated for each decrease in the distance between sources and plotted against their angular distance  $\Delta\theta$ . The resolution capabilities of estimation techniques were assessed with and without the inclusion of preprocessing methods. Altogether, four measurements were performed as described in Table 6.4.

Resulting graphs are shown in Figures 6.7, 6.8 and 6.9.

$\theta_1$ [°]	$\theta_2$ [°]	$\Delta\theta$ [°]	Position offset for $\theta_1$ [m]	Position offset for $\theta_2$ [m]
5	-20	25	0.30	-1.26
-5	-20	15	-0.3	-1.26
-10	-20	10	-0.61	-1.26
-15	-20	5	-0.93	-1.26

Table 6.4: Signal source angles along with required shifts in source positions.

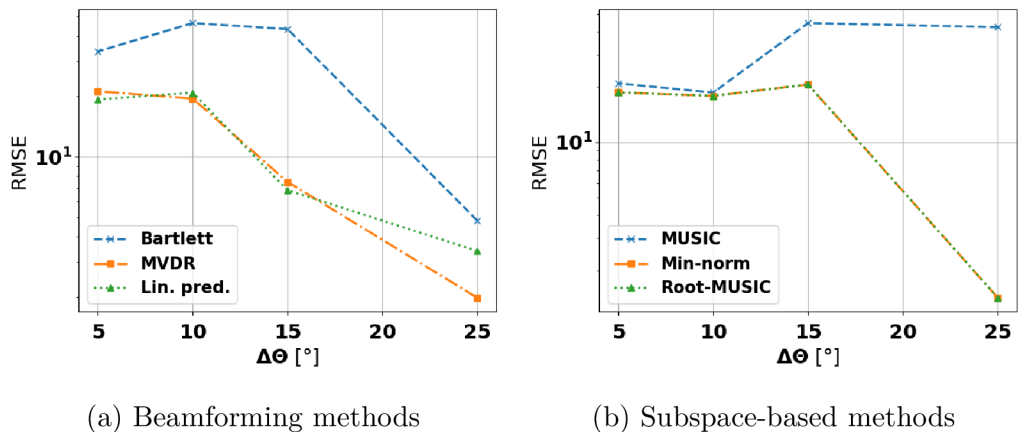
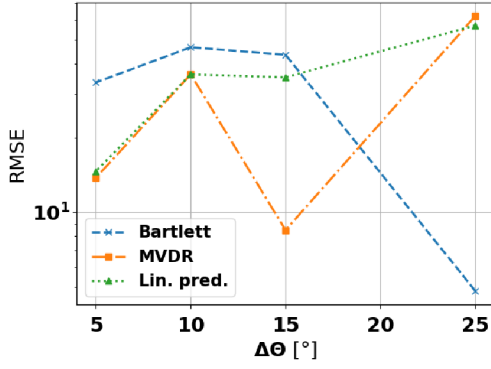


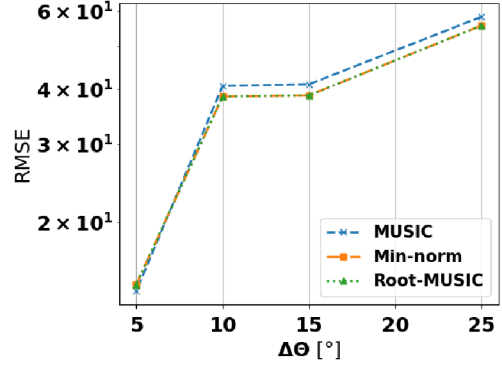
Fig. 6.7: RMSE of estimation techniques based on the angle between two coherent sources.

The measurement results imply that estimation algorithms are unable to provide reliable results in the presence of two highly coherent signals generated by sources located near each other. Signals from sources combine and form a peak in the spectrum somewhere in between angles  $\theta_1$  and  $\theta_2$ , which renders the methods unusable. The peak position is not exactly in the middle because the three-way coaxial adaptor does not split the power equally between the two antennas. Additionally, at lower  $\Delta\theta$ , the two sources seem to behave as a single array with its main lobe steered away from boresight due to phase shifts imposed by varying lengths of coaxial cables. Consequently, the peak in the spectrum is formed in an incorrect direction. Therefore, it makes sense to primarily assess the results for  $\Delta\theta$  from 20 to 25 degrees. An example of this phenomenon is shown in Figure 6.10 for the MUSIC algorithm.

The performance of beamforming methods was assessed first. Bartlett's beamformer is limited by the array's beamwidth. The HPBW of the array can be roughly estimated from the equation [reference the equation in Array fundamentals]:

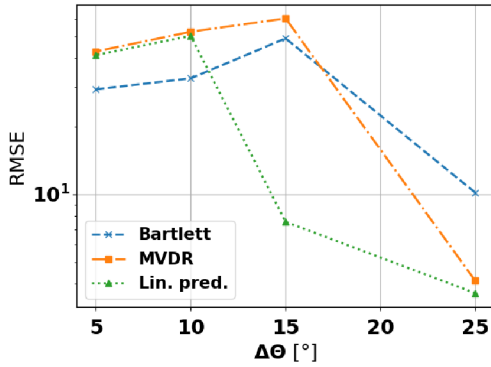


(a) Beamforming methods

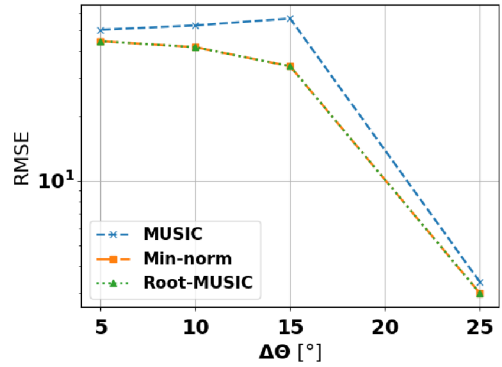


(b) Subspace-based methods

Fig. 6.8: RMSE of estimation techniques with FBA based on the angle between two coherent sources.



(a) Beamforming methods



(b) Subspace-based methods

Fig. 6.9: RMSE of estimation techniques with FB-SS based on the angle between two coherent sources.

$$\begin{aligned} \Theta_{\text{HPBW}} &\approx 2 \left[ \frac{\pi}{2} - \cos^{-1} \left( \frac{1.391\lambda}{\pi Nd} \right) \right] = 2 \left[ \frac{\pi}{2} - \cos^{-1} \left( \frac{1.391 \cdot 0.3}{\pi \cdot 5 \cdot 0.15} \right) \right] = \\ &= 0.356 \text{ rad} = 20.4^\circ \end{aligned}$$

Therefore, the accuracy of the technique decreases rapidly for  $\Delta\theta > 20^\circ$ . The accuracy of the other two methods also decreases, but not as quickly. The FBA method improves the accuracy of the Bartlett beamformer at  $\Delta\theta = 25^\circ$  and fails for MVDR and linear prediction estimation, which corresponds with the simulations. The spatial smoothing reduces the resolution; however, the impact is not as critical as for FBA. Spatial smoothing seems to improve the accuracy of the linear prediction method at higher  $\Delta\theta$ . This, however, might be just a coincidence. Spatial smoothing

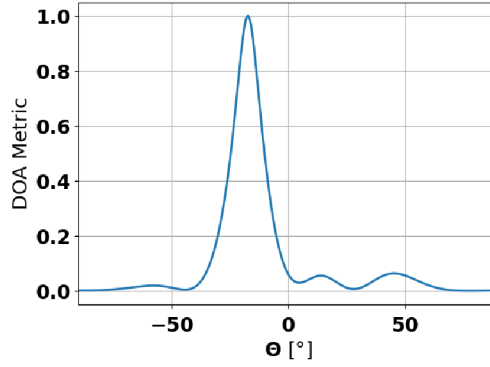


Fig. 6.10: MUSIC spectrum for two coherent sources with 15 degree angular distance.

reduces the resolution of the estimation due to the reduction in array size. Hence, the closer value can be a result of the lower spectral resolution.

The root-MUSIC and min-norm algorithms seem to work even on correlated signals without any preprocessing techniques applied. These methods have proven to be more robust in the presence of correlated sources in comparison with the MUSIC technique. They may potentially provide higher accuracy in signal versus noise subspace differentiation at smaller angular distances between the sources. The FBA fails completely to decorrelate signals for subspace-based methods. The improvement in the resolution at  $\Delta\theta = 5^\circ$  is the result of the signals merging into a singular peak somewhere in the middle between both sources, which means that the maximum error remains at around  $2^\circ$ . Nevertheless, FBA does not prove useful for improving the accuracy of results. Spatial smoothing provides sufficient decorrelation for the MUSIC algorithm to enable estimation at  $\Delta\theta = 25^\circ$ , matching the capabilities of the other subspace-based techniques.

## Conclusion

The aim of the thesis was to perform a study on popular DoA estimation methods, to implement these methods on suitable SDR hardware, and to analyse the performance of the proposed solution against software simulations. DoA estimation algorithms were developed for beamforming and subspace-based techniques for ULA and UCA structures. A description of the proposed hardware and software solution was provided, and estimation algorithms were implemented with the SDR platform. A testbed was built to assess the accuracy of the proposed algorithms, and accuracy tests were conducted. Measurement results were analysed and compared with simulations. In total, six popular estimation algorithms were investigated: Bartlett's beamformer, MVDR, linear prediction, MUSIC, minimum norm, and Root-MUSIC. All the codes used in the thesis are available in the author's GitHub repository [26].

Simulations of various ULA configurations were first performed to assess the effects of changing the array's parameters on the radiation pattern. It was shown that the configuration can be adjusted to a desired use case at the cost of decreased resolution or available scanning range. Next, simulations of proposed DoA estimation methods were assessed based on three metrics: resolution, robustness, and computational complexity.

Resolution was assessed by decreasing the angular distance between two signals impinging on the array from distinct directions. The subspace-based methods outperformed the beamforming methods, maintaining high resolution at much smaller angle differences between signals. The best method proved to be the Root-MUSIC algorithm. Robustness of the methods was first assessed by decreasing the SNR of a single signal impinging on the array. All methods exhibited very similar effects and started to fail at the same SNR level. This was attributed to the simulation of an ideal single-tone signal, which enabled subspace-based techniques to work even in low SNR conditions. Next, the robustness was assessed by simulating two highly coherent signals impinging from distinct directions. Subspace-based methods failed completely without the implementation of any preprocessing techniques. FBA and FB-SS preprocessing techniques enabled subspace-based methods to work in the presence of coherent signals, with FB-SS providing better resolution as SNR levels decreased. The computational complexity of estimation methods was measured by the execution time of simulations. Root-MUSIC was the fastest, while other estimation techniques were four to six times slower in comparison. The performance of Bartlett's beamformer, MVDR, and MUSIC algorithms was tested on a simulated UCA with decreasing SNR levels. Bartlett and MUSIC provided very similar resolution capabilities and outperformed the MVDR algorithm.

The measurements on the proposed testbed setup have demonstrated the func-

tionality of developed estimation algorithms on real-world data samples. The first measurement showed that the accuracy of estimation methods meets the expected resolution, limited by the hardware capabilities. The second measurement indicated that the resolution capabilities in low SNR decrease as the signal source moves towards the array's end-fire direction. The last measurement revealed that all methods failed to accurately resolve the signal locations of two coherent sources even at relatively high angular distances, contrary to the simulations. This discrepancy might be due to both signal sources being connected to a single signal generator, resulting in higher coherence than typically observed in real-world scenarios. Additionally, it was discovered that the absorbers in the anechoic chamber had relatively low attenuation capabilities, likely contributing to signal multi-pathing and thus affecting the measurement accuracy. This issue was further evidenced by the failure of FBA preprocessing for all estimation methods, as FBA is only effective when dealing with two signals impinging on the array simultaneously.

For future measurements, it is recommended to perform measurements in an obstacle-free environment, such as outdoors, to better mitigate the effects of multi-path. Incorporating proper SNR measuring hardware should also be considered to enhance the accuracy of the measurements. Utilising two separate signal generators for generating coherent signals could also improve the measurement accuracy by simulating more accurate real-world coherence conditions.

Future research could extend this work by developing maximum likelihood estimation algorithms and applying the proposed algorithms to more complex array structures. It could also be worthwhile to investigate the potential benefits of the popular ESPRIT estimation technique. Additionally, comparing the performance of the proposed hardware solution to that of a professional-grade DoA estimation setup would be beneficial to verify the feasibility of the hardware for future large-scale solutions.

# Bibliography

- [1] J. Liberti and T. Rappaport, *Smart Antennas for Wireless Communications: IS-95 and Third Generation CDMA Applications*. Prentice Hall communications engineering and emerging technologies series, Prentice Hall PTR, 1999. ISBN: 978-0137192878.
- [2] A. D. Brown, *Active Electronically Scanned Arrays: Fundamentals and Applications*. Wiley, 2022. ISBN: 978-1-119-74905-9.
- [3] “IEEE standard for definitions of terms for antennas,” *IEEE Std 145-2013 (Revision of IEEE Std 145-1993)*, pp. 1–50, 2014.
- [4] C. A. Balanis, *Antenna theory: analysis and design*. Wiley, 2016. ISBN: 978-1-118-64206-1.
- [5] F. Gross, *Smart Antennas with MATLAB, Second Edition*. McGraw-Hill Education, 2015. ISBN: 9780071822381.
- [6] Z. Chen, G. Gokeda, and Y. Yu, *Introduction to Direction-of-arrival Estimation*. Artech House signal processing library, Artech House, 2010. ISBN: 978-1596930896.
- [7] P. Ioannides and C. Balanis, “Uniform circular arrays for smart antennas,” *IEEE Antennas and Propagation Magazine*, vol. 47, no. 4, pp. 192–206, 2005.
- [8] H. L. Van Trees, *Optimum Array Processing: Part IV of Detection, Estimation, and Modulation Theory*. Wiley, 2002. ISBN: 978-0-471-46383-2.
- [9] J. Capon, “High-resolution frequency-wavenumber spectrum analysis,” *Proceedings of the IEEE*, vol. 57, no. 8, pp. 1408–1418, 1969.
- [10] S. Haykin, *Adaptive Filter Theory*. Prentice Hall, 2001. ISBN: 978-0130901262.
- [11] J. Makhoul, “Linear prediction: A tutorial review,” *Proceedings of the IEEE*, vol. 63, no. 4, pp. 561–580, 1975.
- [12] A. Barabell, “Improving the resolution performance of eigenstructure-based direction-finding algorithms,” in *ICASSP '83. IEEE International Conference on Acoustics, Speech, and Signal Processing*, vol. 8, pp. 336–339, 1983.
- [13] H. Krim and M. Viberg, “Two decades of array signal processing research: the parametric approach,” *IEEE Signal Processing Magazine*, vol. 13, no. 4, pp. 67–94, 1996.

- [14] H. Abeida and J.-P. Delmas, “Statistical performance of music-like algorithms in resolving noncircular sources,” *IEEE Transactions on Signal Processing*, vol. 56, no. 9, pp. 4317–4329, 2008.
- [15] T. Collins, R. Getz, A. Wyglinski, and D. Pu, *Software-Defined Radio for Engineers*. Artech House, 2018. ISBN: 978-1-63081-457-1.
- [16] L. Tuta, A. Grivei, I. Nicolaescu, and M. Moni, “Linear antenna array beamforming algorithm for coherent incident signals,” in *2015 23rd Telecommunications Forum Telfor (TELFOR)*, pp. 257–260, 2015.
- [17] A. A. Hussain, N. Tayem, and A.-H. Soliman, “Low complexity doa estimation of multiple coherent sources using a single direct data snapshot,” *IEEE Access*, vol. 12, pp. 2371–2388, 2024.
- [18] M. Krueckemeier, F. Schwartau, C. Monka-Ewe, and J. S. Technische, “Synchronization of multiple usrp sdrs for coherent receiver applications,” in *2019 Sixth International Conference on Software Defined Systems (SDS)*, pp. 11–16, 2019.
- [19] M. Bartolucci, J. A. Del Peral-Rosado, R. Estatuet-Castillo, J. A. Garcia-Molina, M. Crisci, and G. E. Corazza, “Synchronisation of low-cost open source sdrs for navigation applications,” in *2016 8th ESA Workshop on Satellite Navigation Technologies and European Workshop on GNSS Signals and Signal Processing (NAVITEC)*, pp. 1–7, 2016.
- [20] C. Laufer, *The Hobbyist’s Guide to the RTL-SDR: Really Cheap Software Defined Radio*. Wiley series in software radio, CreateSpace Independent Publishing Platform, 2015. ISBN: 978-1514716694.
- [21] M. Laakso, R. Rajamäki, R. Wichman, and V. Koivunen, “Phase-coherent multichannel sdr - sparse array beamforming,” in *2020 28th European Signal Processing Conference (EUSIPCO)*, pp. 1856–1860, 2021.
- [22] M. Laakso, *Multichannel coherent receiver on the RTL-SDR*. M.sc. thesis, Sch. of Electrical Engineering, Aalto Univ., Espoo, FI, 2019. Available at <https://aaltodoc.aalto.fi/handle/123456789/37163>, [cited 2024-05-17].
- [23] S. Skinner, K. Patel, J. Pittman, B. Lebednik, F. Vassallo, and K. J. Duncan, “Direction finding system using an n-channel software defined radio implemented with a phase interferometry algorithm,” in *2019 SoutheastCon*, pp. 1–5, 2019.



- [24] N. BniLam, D. Joosens, M. Aernouts, J. Steckel, and M. Weyn, “Loray: Aoa estimation system for long range communication networks,” *IEEE Transactions on Wireless Communications*, vol. 20, no. 3, pp. 2005–2018, 2021.
- [25] S. Hüsge, M. Meuleners, and C. Degen, “An inexpensive sdr system for emitter localization,” in *2021 18th European Radar Conference (EuRAD)*, pp. 245–248, 2022.
- [26] D. Sedláček, “Software-defined antenna array for signal direction of arrival estimation.” GitHub repository, 2024. Available online: [https://github.com/SedlacekDavidTN/Masters\\_thesis](https://github.com/SedlacekDavidTN/Masters_thesis), [cited 2024-05-20].
- [27] KrakenSDR, “Antenna array setup.” GitHub repository, 2024. Available online: [https://github.com/krakenrf/krakensdr\\_docs/wiki/04.-Antenna-Array-Setup](https://github.com/krakenrf/krakensdr_docs/wiki/04.-Antenna-Array-Setup), [cited 2024-05-17].

# Symbols and abbreviations

<b>ADC</b>	Analog-to-Digital Converter
<b>AESA</b>	Active Electronically Scanned Array
<b>AoA</b>	Angle-of-arrival
<b>DAQ</b>	Data Acquisition
<b>DoA</b>	Direction-of-Arrival
<b>DSP</b>	Digital Signal Processing
<b>ESA</b>	Electronically Scanned Array
<b>EVD</b>	Eigenvalue Decomposition
<b>FBA</b>	Forward-Backward Averaging
<b>FB-SS</b>	Forward-Backward Spatial Smoothing
<b>FFT</b>	Fast Fourier Transform
<b>HPBW</b>	Half-Power Beamwidth
<b>IF</b>	Intermediate Frequency
<b>LNA</b>	Low-Noise Amplifier
<b>LO</b>	Local Oscillator
<b>MDL</b>	Minimum Descriptive Length
<b>ML</b>	Maximum-Likelihood
<b>MUSIC</b>	Multiple Signal Classification Technique
<b>MVDR</b>	Minimum Variance Distortion-less Response
<b>PESA</b>	Passive Electronically Scanned Array
<b>RF</b>	Radio Frequency
<b>RFFE</b>	Radio Frequency Front-End
<b>RMSE</b>	Root Mean Square Error
<b>RPi</b>	Raspberry Pi

<b>SDR</b>	Software-defined radio
<b>SNR</b>	Signal-to-Noise Ratio
<b>SVD</b>	Singular Value Decomposition
<b>ULA</b>	Uniform Linear Array
<b>UCA</b>	Uniform Circular Array
<b>VM</b>	Virtual Machine